Proposed PMSG and Model Analysis

2.1. Introduction

In chapter 1, it is discussed that wind power is the most suitable and sustainable sources of energy. The PMSG is found most suitable for the direct drive wind turbine generator. The dual stator or rotor PMSG is having high power density and high efficiency than single stator single rotor PMSG. The multi-phase systems are preferable choice because of high fault tolerant capability, reliability and high power density. For design optimization of a generator, analytical method based on magnetic circuit is the simplified suitable choice than finite element method (FEM) because it saves the time and model complexity.

In this Chapter, a novel dual stator multi-phase PMSG is proposed and reluctance network model method is opted for the design analysis. A comparison between the dual stator annular rotor and novel magnetically coupled PMSG is discussed in Section 2.2. The basics of winding, winding feasibility and details of winding of the proposed generator are discussed in Section 2.3. The core material and their selection process are discussed in Section 2.4 and rotor PM sleeve selection is discussed in Section 2.5. The rating and specification of both the proposed PMSG are discussed in Section 2.6. The improved magnetic circuit (IMC) of single stator five phase PMSG (SSFP-PMSG) is discussed in Section 2.7 and their finite element method model is discussed in Section 2.8. The results and result verification are discussed in Section 2.9. The IMC for MCDSFP-PMSG are discussed in Section 2.10 followed by FEM analysis and result validation in Section 2.11. Finally, Chapter has been concluded in section 2.12.

2.2. Dual stator cup type rotor PMSG Versus Novel Magnetically coupled Dual stator PMSG

The Dual stator five phase PMSG has an annular or cup type rotor. It is placed in between the inner and the outer stator. Eight magnetic poles made of similar grade magnetic material (NdFeB) are arranged on each side of the rotor. There are three possible flux paths - two are local and one is coupled flux path, as shown in Fig. 2.1. Local flux de-rates the machine while coupled flux decides the performance of the machine. The adjacent magnets are placed such that flux lines corresponding to common useful flux ($\varphi_{cf}/2$) for both the magnets are in the same direction. This establishes a magnetic coupling, which adds up the MMF of the inner magnet and the outer magnet. The common flux is established in the air-gap of both inner and outer stator as MMFs are additive in nature. To limit the leakage fluxes, flux barrier in the local paths is set up, as shown in Fig. 2.2. By restricting the leakage flux, the barrier enhances the useful flux. Flux barrier divides the rotor into eight symmetrical segments. These segments may be either double T-shaped or Tapered shaped. The Tapered shape is preferred due to better aerodynamics and less mechanical complexity. To minimize leakage flux and harmonics in the induced electromotive force, the flux barrier width needs to be optimized. This is decided by the separation angle (α) of the segmented rotor, whose optimized value is discussed in Section 2.11. The importance of this novel technique for magnetic coupling in dual stator PMSG is identified here for the very first time.
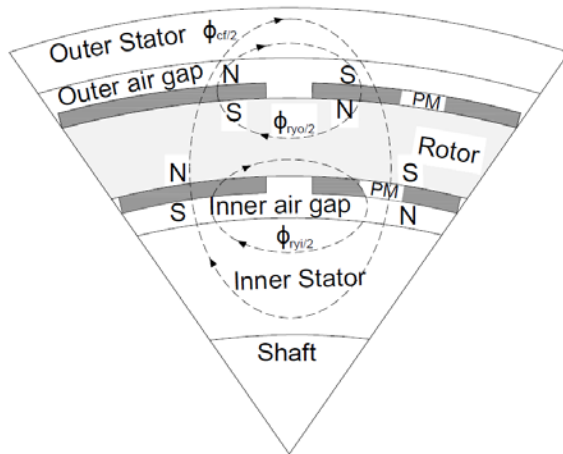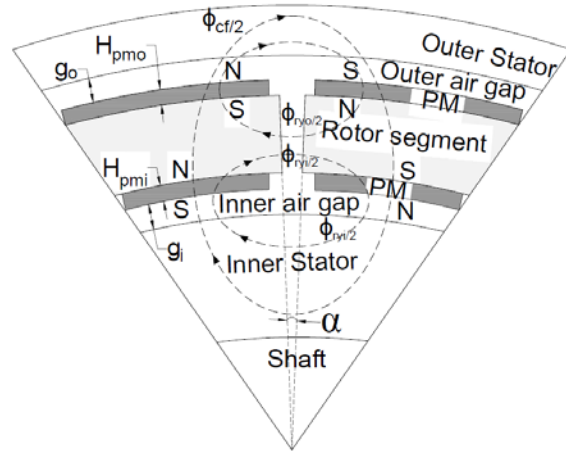
Fig. 2.1 Rotor without segmentation   Fig. 2.2 Rotor with segmentation

2.3. Stator Winding of PMSG

The winding is the main component of any electrical machine. It is popularly made-up with metal like copper and aluminum. Though aluminum is cheaper and light in weight (around 30% of copper), the copper is mainly preferred for winding because it has 42.76% higher conductivity and around 56.2% higher tensile strength than aluminum.

The copper wire is coated with different insulating materials according to their maximum allowable operating temperature as listed in Table 2.1.

Table 2.1: Winding insulation

Insulation Material	Maximum Attainable Temperature (^{O}C)
Class Y	90
Class A	105
Class E	120
Class B	130
Class F	155
Class H	180
Class C	> 180

The winding can be classified into two categories namely non-overlap winding and overlap winding. The non-overlap winding is the concentrated winding whereas the overlapping winding can be either concentrated or distributed. The non-overlap winding is preferred where the space for overhang winding is limited because the concentrated winding possesses less overhang of the winding. Although the concentrated winding is compact and requires less copper for winding, it contains odd harmonic in the generated voltage. Thus the %THD of generated voltage of such winding is higher than distributed winding. The non-overlap winding 20 slots, 5-phase, 8 poles and 0.5 slots per pole per phase (spp) is concentrated winding whereas overlap winding 60 slot, 5-phase, 8 poles and 1.5 spp is distributed winding.

The main drawback of concentrated winding is their lower value of winding factor than distributed winding. For the 60 slot, 5-phase, 8poles winding the winding factor is 0.9878 whereas, for the 20 slot, 5-phase, 8 poles winding the winding factor is 0.951. The lesser winding factor requires more magnetic flux in the air-gap for achieving the same power rating. Therefore, distributed winding is used in the proposed machine.

2.3.1. Stator Winding Feasibility

There are various combinations of slots and poles possible but all combination cannot provide the valid balance winding. Only those combinations of slot and poles give the valid balanced winding, whose phase offset value is an integer. It can be determined by Eqn. (2.1) [136].

$$\theta_{pa} = rem\left(k \frac{N_m}{N_s} 180^o E, 360^o E \right) \qquad (2.1)$$

Where θ_{pa} is the principle angle (360/No. of phase), N_m is the no of magnetic poles, N_s is the no. of stator slots and k is the phase offset which has an integer value less than the total number of slots.

There are various slot combinations (outer and inner) possible corresponding to a 5 phase machine. But the choice of cores having 60 slots for outer stator and 20 slots for inner stator are based on availability of resources. A possible feasible combination of slot and pole winding are shown in Table 2.2. The ($\surd$) is used for feasible and (X) is used for not feasible winding with that slot and pole combinations.

According to the slots and pole combination only 60 slots, 10 poles, and 20 slots, 10 poles winding are not feasible. From all the possible combinations of slots and poles, 60 slots, 8 pole and 20 slots, 8 poles are taken for the proposed PMSG.

Table:2.2 Winding Feasibility

Poles	4	6	8	10	12	14
No. of Outer Stator Slots	60	60	60	60	60	60
Outer Stator Winding Feasibility	$\surd$	$\surd$	$\surd$	X	$\surd$	$\surd$
No. of Inner Stator Slots	20	20	20	20	20	20
Inner Stator Winding Feasibility	$\surd$	$\surd$	$\surd$	X	$\surd$	$\surd$

There are two five phase PMSG proposed in this Chapter namely single stator single rotor five phase PMSG (SSFP-PMSG) and Dual stator single rotor five phase PMSG (MCDSFP-PMSG). For the SSFP-PMSG, 60 slots and 8 poles winding is considered and for the MCDSFP-PMSG, 60 slots and 8 poles are considered for the outer stator and 20 slots and 8 poles are for the inner stator winding.

The winding details of both the PMSGs are described below in detail:

The SSFP-PMSG consists of a stator and permanent magnet rotor. The 60 slot, 8 pole, 5 phase double layer fractional slot windings with the 72^oE phase difference between adjacent phases are placed in the stator. It consists of 240 turns in 12 coils per phase which are shown in Fig. 2.3. Coils are short-pitched by 12^oE that eliminates the higher order harmonics in the generated voltage and also reduces conductor copper loss and effective weight of the machine. The color of phases is red, green, blue, yellow and black for A, B, C, D and E phases, respectively. This winding arrangement suppresses the higher order harmonics and reduces the copper requirement.

Double layer fractional slot distributed winding used in this design are having smaller end winding compared to single layer winding. This reduces the copper requirement and it eliminates space harmonics. The inner and outer stator winding are having 0.5 and 1.5 SPP, respectively. For this arrangement, the inner winding creates short pitching of 36^oE (electrical) and outer winding creates 12^oE short pitching. These short pitching suppress multiple of 5th order harmonics in inner stator and multiple of 15th order harmonics in the outer stator winding. It is important to mention that, to avoid under utilization of magnets, the inner and outer magnets are purposely short-pitched. The distribution factor of the inner stator winding is 1, which makes it behave like concentrated winding, whereas the outer stator winding having distribution factor 0.993 behaves like distributed winding. Since space is restricted for the overhang of inner winding hence its concentric nature is more suitable. Therefore, the outer stator winding has more sinusoidal MMF distribution and consequently, the outer EMF is also more sinusoidal than inner stator winding. The winding pattern of inner and outer stator windings for phase-A is shown in Fig. 2.4. The phase spread of inner stator winding is

zero; thus generated voltage of all the four coils is added together, while for the outer stator winding phase spread is 24° E; therefore the generated voltage of all the 12-coils/phase are added together by taking into account their phase angles.
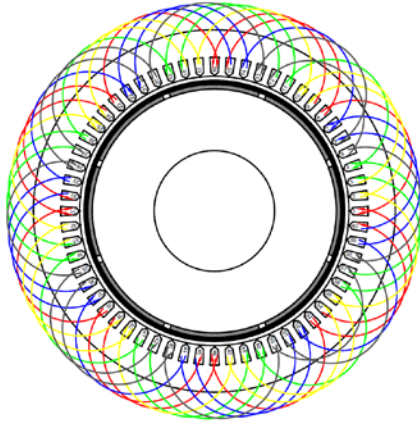

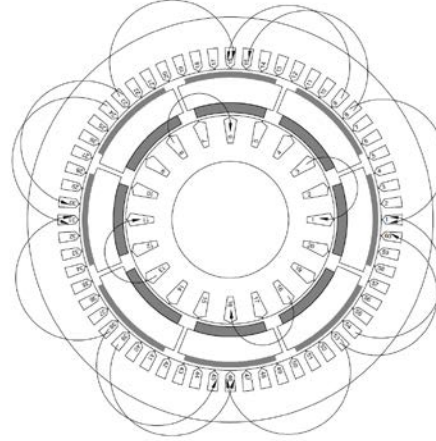Fig. 2.3 Five Phase Winding Pattern of SSFP-PMSG

Fig. 2.4 Winding Layout of A-phase for MCDSFP-PMSG

2.4. Core Material

Stator and rotor core are made up with thin laminations of a soft magnetic material alloy called dynamo grade for the minimum hysteresis loss with high-grade silicon steel alloy, as shown in Fig. 2.5. This material has advantages of high permeability, low coercivity, and narrow hysteresis loops. These laminations are insulated from each other with high thermal resistant varnish. This insulating material depends on the maximum allowable temperature as shown in Table 2.3.

Table 2.3: Yoke insulation materials

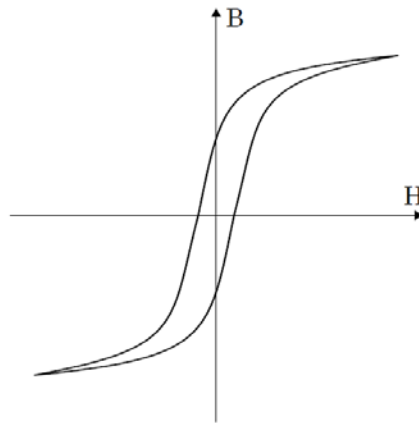| Material (Silicon resins laminated)	Temperature (^{O}C)
Class A (Impregnated Varnished)	105 (max.)
Class B	130-155
Class F	155-180
Class H	180-200

Fig. 2.5 Hysteresis Loop of Soft Magnetic Material

The composition of iron (95 to 97%) with silicon (2 to 3.5%) alloy reduces the electrical conductivity, which develops smaller eddy current loss in the lamination of the core. Further, the loss can be reduced with the use of amorphous steel alloy for high-frequency application [137]. It has the advantage of very high magnetic permeability, high fracture toughness and high resistivity [138]. For high flux density machine, air core is preferred due to saturation in iron core [139]. To understand the effect of core material on flux distribution and performances, four core materials are considered as listed in Table 2.4. The flux distribution can be evaluated using analytical and finite element method (FEM) with these core materials.

Table 2.4: Different core materials

Parameters	Relative Permeability	Resistivity (Ω.m)
Cast iron	100	$100*10^{-8}$
Air	1.00000037	$2*10^{16}$
Amorphous steel alloy	10000	$130*10^{-8}$
Silicon steel alloy	5500	$45*10^{-8}$

.

2.5. Rotor PM Sleeve Material

A strong PM sleeve is required to retain the segmented magnets. It counter balances the centrifugal as well as inter-magnet repulsive forces. Therefore, aluminum (Al), copper, magnetic stainless steel and carbon/glass fiber are used for this purpose. Except for carbon/glass fiber, others are easy to machine and assemble but they possess high electrical conductivity and cause significant eddy current loss [140]. On the other hand, carbon/glass fiber is light and strong with low electrical conductivity. However, it has less thermal conductivity and occupies a larger volume of the rotor. Despite it is quite suited for high-frequency application [141]. The drawback of eddy current loss in metallic sleeves could be avoided using a low cost porous metallic sleeve having similar strength. There are four materials listed in Table 2.5 are considered to know the effect of sleeve material on the magnetic flux distribution. The flux distribution can be evaluated using the analytical method and FEM with these rotor sleeve materials. The permeability of the non-magnetic rotor sleeves (Al, copper, carbon fiber) are approximately the same but have different electrical resistivity.

Table 2.5: Different sleeve materials

Parameters	Relative Permeability	Resistivity (Ω.m)
Al	1.000022	$2.65*10^{-8}$
Copper	0.999994	$1.724*10^{-8}$
Carbon fiber	1	$3*10^{-5}$
Stainless steel	95	$6.9*10^{-7}$

2.6. Permanent Magnet Material

Permanent magnet material is made up of hard magnetic material having a high value of coercivity (Hc) and high remanent flux density (Br) as shown in Fig. 2.6. The NdFeB magnets are used in the proposed PMSG due to the high value of (BH)max and low cost compared to SmCo permanent magnets. The different grade of NdFeB permanent magnet material with the maximum allowable temperature are shown in Table 2.6.

Table 2.6: Different grade of NdFeB permanent magnet

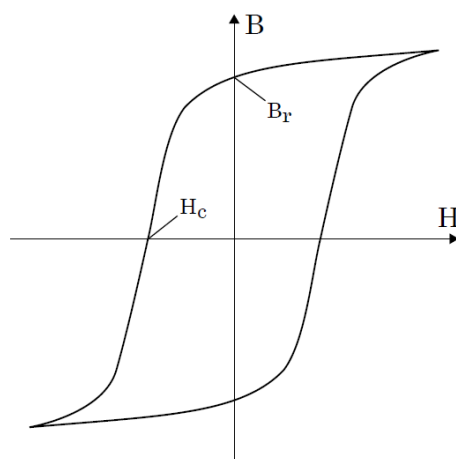| PM material	Maximum operating Temperature (^{O}C)
NdFeB N	80
NdFeB M	100
NdFeB H	120
NdFeB SH	150
NdFeB UH	180
NdFeB EH	200

Fig. 2.6 B-H curve of permanent Magnet material

2.6.1. Specifications of Proposed Permanent Magnet Generator

From Section 2.2, it is found that the Novel magnetically coupled dual stator are having better performance than dual stator annular rotor PMSG. From section 1.5 it is found that multi-phase winding enhances the power density, reliability and fault-tolerance capability. To further enhance power density, reliability and fault tolerance, both the approaches are combined together to produce a Novel magnetically coupled dual stator five phase PMSG (MCDSFP-PMSG). At first, a single stator PMSG is analyzed due to its simpler structure and better reliability. After that, MCDSFP-PMSG is analyzed to have better power density as compared to a single one.

Fig. 2.7 shows the schematic model of 60 slots, 8 poles SSFP-PMSG. It consists of stator and surface mounted permanent magnet rotor. The stator core houses the five-phase double layer fractional slot short-pitched winding. The specifications of SSFP-PMSG are listed in Table 2.7.

The schematic of the MCDSFP-PMSG is presented in Fig. 2.8. It consists of two stators and one segmented rotor. The outer stator consists of 60 slots whereas inner stator 20 slots, which are occupied by the two sets of five phases, balanced double layer windings. The two sets of 8 permanent magnets are placed on both the inner and outer surfaces of the segmented annular rotor. The specifications of MCDSFP-PMSG are listed in Table 2.8.
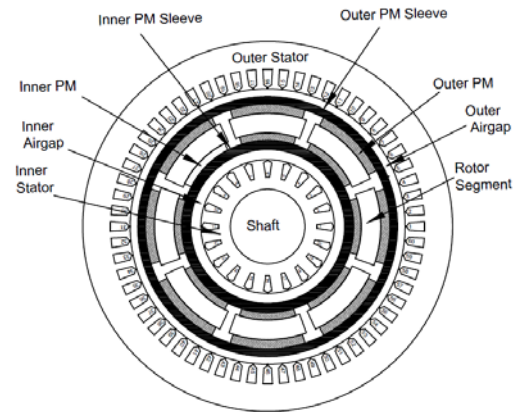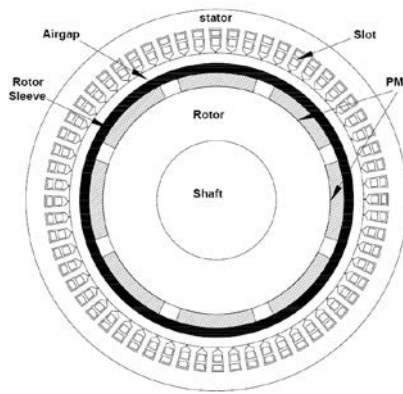
Fig 2.7 Schematic of single stator single rotor generator

Fig 2.8 Schematic of MCDSFP-PMSG

Table 2.7: The specifications of the SSFP-PMSG

Parameter	Value
Power (KVA)	3.878
Voltage (Volt.)	193.92
Current (Amp.)	4
Speed (RPM)	400
Axial Length	95 mm
Radius of Shaft	20 mm
Outer radius of the rotor	95 mm
Height of magnet	2.5 mm
Air-gap length	2.0 mm
Rotor sleeve thickness	0.5 mm
Inner radius of stator	100 mm
Outer radius of stator	175 mm
Area of slot	125 mm^2

Table 2.8: The specifications of the MCDSFP-PMSG

Parameter	Value
Power (KVA)	5.12

Outer stator voltage (Volt.)	224
Inner stator voltage (Volt.)	32
No. of Phases	5
Current (Amp.)	4
Speed (RPM)	400
Axial Length	125 mm
Radius of shaft	14 mm
Outer radius of inner stator	47.2 mm
Air-gap Inner or Outer	2.0 mm
Thickness of rotor sleeves	0.5 mm
Width of rotor yoke	42.8 mm
Inner radius of outer stator	100 mm
Outer radius of outer stator	175 mm
Area of inner stator slot	98 mm^2
Area of outer stator slot	125 mm^2
No. of inner stator slot	20
No. of outer stator slot	60
Inner and Outer magnet	8

2.7. Improved Magnetic Circuit Model of Air-gap flux for SSFP-PMSG

The SSFP-PMSG has 8 poles on the rotor and permanent magnets are contained by the rotor sleeve. There are three flux paths, one for the main air-gap and other two for leakage flux, shown in Fig. 2.9. The useful flux decides the rating of the machine whereas the leakage flux injects harmonics. The two leakage fluxes are magnet to

magnet and magnet to the rotor. The magnet to magnet leakage flux can be bifurcated in to two, one through air-gap and the other through rotor sleeve. Their magnitude depends on the material of the rotor sleeve.
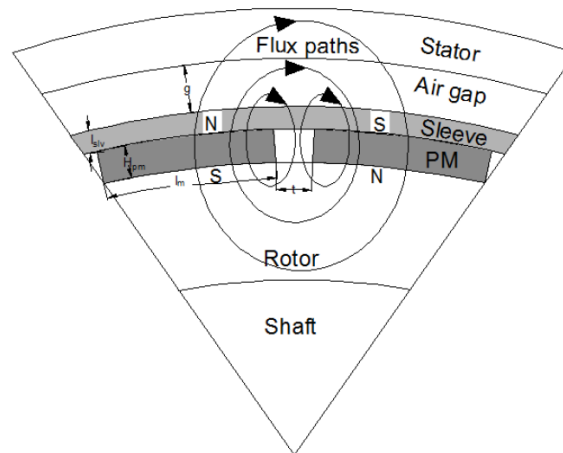

Fig. 2.9 SSFP-PMSG model

The improved magnetic circuit (IMC) model is developed for the SSFP-PMSG. It is presented for computing leakage and main flux, as shown in Fig.2.9. Since this machine has quarter symmetry so only one-fourth part of the model is shown in the figure. Analogous to the Ohm's law, the equivalent magnetic circuit for the IMC model is presented in Fig. 2.10.

This network consists of two MMF sources and reluctance of various parts of the model. MMF sources are five phase winding and permanent magnets. For accurate prediction of flux distribution this model includes reluctance of various sections of the machine-air-gap (R_g), permanent magnet (R_{pm}), stator yoke (R_{sy}), stator tooth (R_{ste}), rotor core (R_r), rotor sleeve (R_{sl}), magnet to rotor (R_{ml}), magnet to magnet due to air (R_{mam}) and magnet to magnet through flux conducting sleeve (R_{mslm}). This network consists of two MMF sources and reluctance of various parts of the model. MMF sources are five phase winding and permanent magnets.
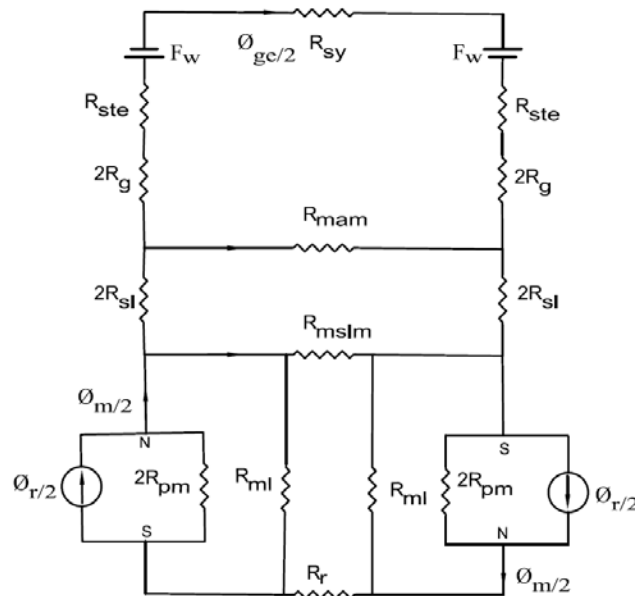
Fig. 2.10 Improved magnetic circuit model of SSFP-PMSG

For accurate prediction of flux distribution this model includes reluctance of various sections of the machine-air-gap (R_g), permanent magnet (R_{pm}), stator yoke (R_{sy}), stator tooth (R_{ste}), rotor core (R_r), rotor sleeve (R_{sl}), magnet to rotor (R_{ml}), magnet to magnet due to air (R_{mam}) and magnet to magnet through flux conducting sleeve (R_{mslm}). The reluctance changes as permeability depend on the material. For different sections, the flux corresponds to air-gap φ_{ge}, the surface of permanent magnet φ_m, flux sources φ_r, leakage magnet to rotor φ_{mr}, leakage magnet to magnet via air φ_{mam}, leakage magnet to magnet through sleeve φ_{mslm}. All these elements are shown in Fig. 2.10. Since there are two MMF sources, so for the network analysis, principle of superposition is opted. At no-load, only PMs are the MMF sources that is shown in Fig. 2.11. Since PM is the main flux source, therefore this model is used for optimization and the extraction of no-load characteristics.
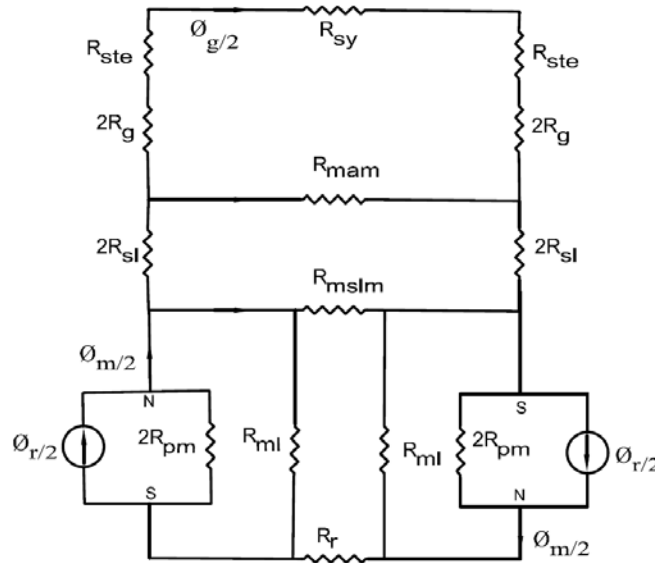
Fig. 2.11 Improved magnetic model for no-load of SSFP-PMSG

MMF due to armature reaction of five phase winding is the other source which appears under loading conditions. The effect of this MMF source can be calculated separately by short-circuiting the other PM MMF sources and replacing them with their series reluctance as shown in Fig. 2.12.
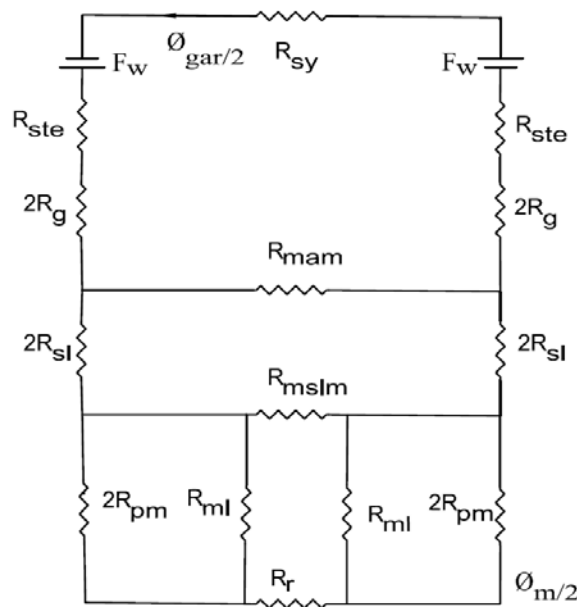
Fig. 2.12 Improved magnetic model with winding mmf of SSFP-PMSG

To develop the analytical expression using IMC for the prediction of flux distribution, the leakage factors taken into consideration are

$$\alpha = \frac{R_{pm}}{R_{ml}} \tag{2.1}$$

$$\beta = \frac{R_{pm}}{R_{mam}} \tag{2.2}$$

$$\gamma = \frac{R_{pm}}{R_{mslm}} \tag{2.3}$$

2.7.1. Permeance Calculation for Magnet to Magnet Leakage Path

The permeance of magnet to magnet leakage flux path is calculated using circular arc-straight technique [136]. In this technique, flux path is divided into two curves: fringing flux length is circular arc and air-gap length between the magnets is straight line. The leakage flux has two paths, one from magnet-rotor sleeve-magnet, and other from magnet-air-magnet. Therefore the two permeances are in series which are calculated on the basis of their dimensions and material properties. Fig. 2.13 shows the path of leakage flux between magnet to magnet through air and rotor sleeve.

The permeance of magnet to magnet leakage flux path through rotor sleeve (P_{mslm})

$$P_{mslm} = \int_0^{l_{sl}} \frac{\mu_0 \mu_{sl} L}{\delta + \pi \zeta} d\zeta = \frac{\mu_0 \mu_{sl} L}{\pi} ln(1 + \frac{\pi l_{sl}}{\delta}) = \frac{1}{R_{mslm}} \tag{2.4}$$

The permeance of magnet to magnet leakage flux path through air (P_{mam})

$$P_{mam} = \int_{l_{sl}}^{g_e} \frac{\mu_0 L}{\delta + \pi \zeta} d\zeta = \frac{\mu_0 L}{\pi} ln(\frac{\delta + \pi g_e}{\delta + \pi l_{sl}}) = \frac{1}{R_{mam}} \tag{2.5}$$
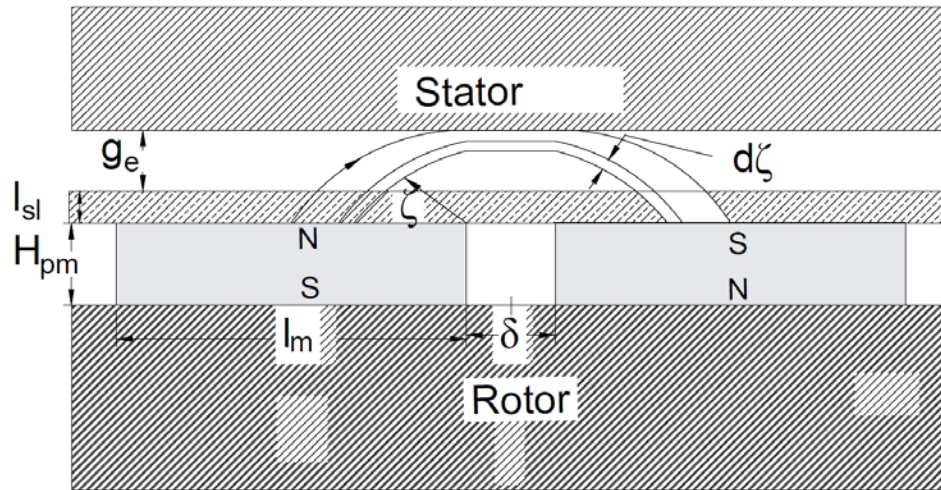
Fig. 2.13 Magnet to magnet leakage flux path

2.7.2. Permeance Calculation for Magnet to Rotor Iron Leakage Path

Using circular arc-straight technique, Fig. 2.14 shows the path of leakage flux between magnet and rotor iron.

The permeance of magnet to rotor iron leakage flux path

$$P_{mi} = \int_0^{g_e} \frac{\mu_0 L}{H_{pm} + \pi\zeta} d\zeta = \frac{\mu_0 L}{\pi} ln(1 + \frac{\pi g_e}{H_{pm}}) = \frac{1}{R_{mi}} \qquad (2.6)$$
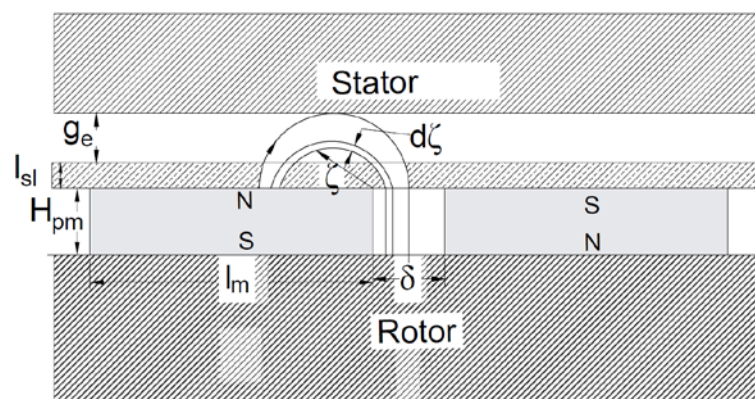

Fig. 2.14 Magnet to rotor iron leakage flux path

Leakage parameter in terms of physical dimension

$$\alpha = \frac{H_{pm}}{\pi\mu_{pm}l_m}ln(1+\frac{\pi g_e}{H_{pm}})$$ (2.7)

$$\beta = \frac{H_{pm}}{\pi\mu_{pm}l_m}ln(\frac{\delta+\pi g_e}{\delta+\pi l_{sl}})$$ (2.8)

$$\gamma = \frac{\mu_{sl}H_{pm}}{\pi\mu_{pm}l_m}ln(1+\frac{\pi l_{sl}}{\delta})$$ (2.9)

The following reduced expression is derived in term of machine dimensions and

magnetic properties [142].

The reluctance of Air gap (Rg)

$$R_g = \frac{g_e}{\mu_0(l_m + 2g_e)L}$$ (2.10)

The reluctance of permanent magnet (Rpm)

$$R_{pm} = \frac{H_{pm}}{\mu_0\mu_{pm}l_m L}$$ (2.11)

The reluctance of stator yoke (Rsy)

$$R_{sy} = \frac{l_{sy}}{2\pi\mu_0\mu_{fe}r_s\theta_p L_i}$$ (2.12)

The reluctance of stator tooth (Rste)

$$R_{ste} = \frac{h_\delta}{\mu_0\mu_{fe}w_t L_i}$$ (2.13)

The reluctance of rotor yoke (Rr)

$$R_r = \frac{l_{ry}}{2\pi \mu_o \mu_{fe} r_r \theta_p L_i}$$

(2.14)

2.7.3. Magnetic Circuit Parameters and Fluxes under No-Load

Using the above-mentioned reluctance parameters, the IMC shown in Fig. 2.11 is simplified to Fig. 2.15 and further reduced to Fig. 2.16.
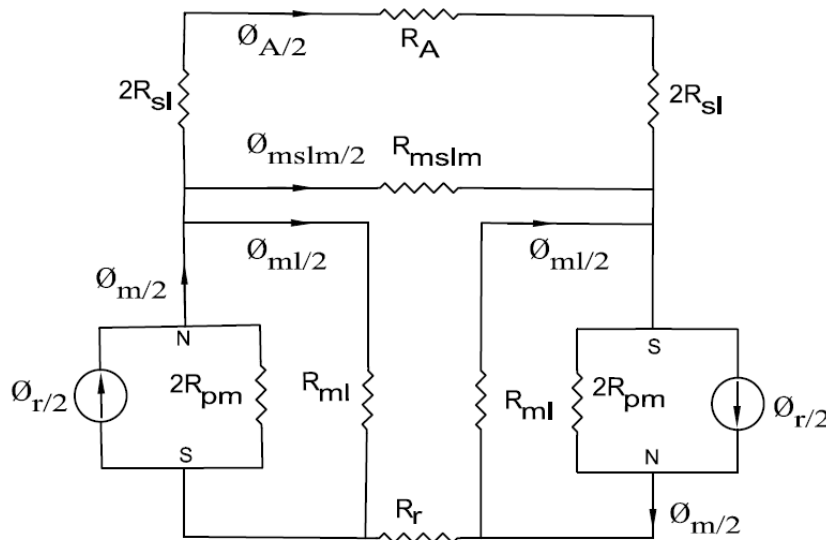

Fig. 2.15 Simplified form of IMC

The reluctance of various sections after simplification

$$R_A = \frac{R_D}{R_{pm} + \beta R_D}$$

(2.15)

Where

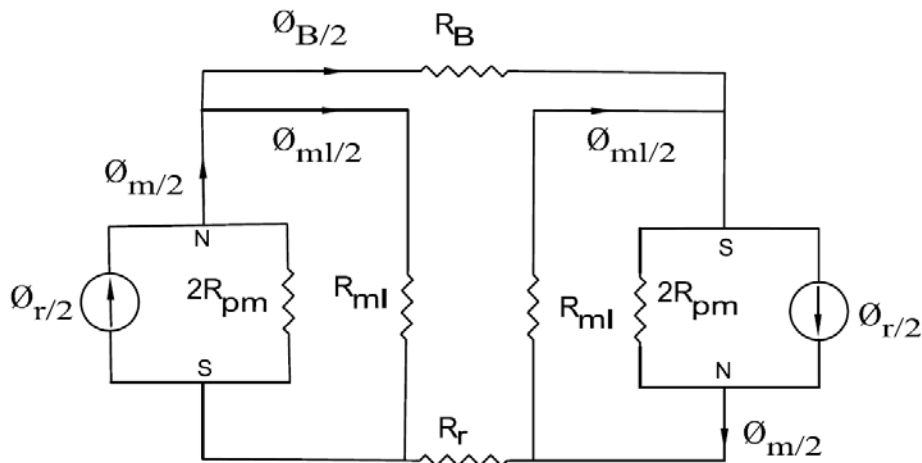$$R_D = R_{sy} + 4R_g + 2R_{ste}$$

(2.16)

Fig. 2.16 Reduced form of IMC

$$R_B = \frac{R_E + R_{pm}}{\gamma R_E + R_{pm}(R_{pm} + \beta R_D)} \qquad (2.17)$$

Where,

$$R_E = R_D R_{pm} + 4R_{sl}(R_{pm} + \beta R_D) \qquad (2.18)$$

Flux through the surface of the permanent magnet (φ_m)

$$\varphi_m = \frac{4R_{pm} + 2\alpha R_F(1 + 2\alpha)}{R_F(1 + 2\alpha)^2}\varphi_r \qquad (2.19)$$

Where,

$$R_F = R_B + 2R_C + R_r \qquad (2.20)$$

$$R_C = \frac{2R_{pm}}{1 + 2\alpha} \qquad (2.21)$$

Air gap flux (φ_g)

$$\varphi_g = \frac{4R_{pm}^3}{(R_{pm} + \beta R_D)(R_{pm} + \gamma(R_A + 4R_{sl}))R_F(1 + 2\alpha)}\varphi_r \qquad (2.22)$$

2.7.4. Magnetic Flux Densities

Air gap flux density (B_g)

$$B_g = \frac{4R_{pm}^3 C_\phi}{(R_{pm} + \beta R_D)(R_{pm} + \gamma(R_A + 4R_{sl}))R_F(1 + 2\alpha)} B_r \qquad (2.23)$$

Where C_ϕ is the flux concentration factor of the air gap.

Flux density on the surface of the permanent magnet (B_m)

$$B_m = \frac{4R_{pm} + 2\alpha R_F(1 + 2\alpha)}{R_F(1 + 2\alpha)^2} B_r \qquad (2.24)$$

2.7.5. Electromagnetic Performance

The magnetic flux distribution in air-gap due to arc-shaped magnets is flat-topped. This is because of odd harmonic components. Equation (2.25) presents the fundamental and harmonic component of magnetic flux distribution in air-gap.

Magnetic flux density due to PMs in the air-gap

$$B_g(\theta_{er}) = \int_{k=1,3,5}^{\infty} B_{gk} \sin(k\theta_{er}) \qquad (2.25)$$

Where the peak value of flux density (Bgk) is

$$B_{gk} = \frac{4}{\pi(\frac{\pi}{2} - \beta)} \frac{B_g}{k^2} \cos(k\beta) \sin(k\frac{\pi}{2}) \qquad (2.26)$$

The generated electromotive force (EMF) is the rate of change of flux linkage in the winding with respect to time. In each phase winding, there are 12 short-pitched coils distributed at the periphery of the stator core. The generated voltage per phase is the phasor sum of the voltages generated in each of these coils. Equation (2.27) is the generated voltage per phase in the machine considering fundamental and harmonics.

$$E(t) = \sum_{k=1,3,7}^{\infty} E_k \sin(kw_e t) \tag{2.27}$$

Where,

$$E_k = \frac{16}{P} \times 2.9563 \times N_c L_i r_s w_e B_{gk} \cos(k\frac{\pi}{30}) \tag{2.28}$$

The cogging torque is a serious drawback of PM machines which needs to be monitored. It occurs due to the interaction of rotor magnets and stator teeth [143]. The reluctance of air-gap varies periodically with rotor rotation. Its periodicity depends on the number of stator slots. In contrast, the flux in the air-gap is also a periodic and its periodicity depends on the number of magnets on the rotor. The periodicity of cogging torque depends on the least common multiple of the number of stator slots and number of rotor poles [144].

The cogging torque developed in the machine.

$$T(cogg) = \sum_{q=0}^{\infty} T_q \sin(uq\theta) \tag{2.29}$$

Where u is the least common multiple of the number of stator slots and number of rotor poles, q is an integer and Tq is the Fourier coefficient of cogging torque.

2.7.6. MMF Calculation due to Five-Phase Winding

Under loading conditions, there are two MMF sources as shown in Fig. 2.10. The MMF due to PM depends on the material properties and its dimensions which is already discussed whereas the winding MMF which needs to be calculated, is dependent on the actual distribution of winding in slots and the phase currents. To calculate the actual winding distribution, the winding function approach is opted.

The winding function is given as

$$N(\theta_e) = n(\theta_e) - < n(\theta_e) > \tag{2.30}$$

where $n(\theta_e)$ represents the turn function of winding. The winding function can be represented as

$$N(\theta_e) = \begin{cases} \dfrac{22}{15}N_c & 0 \le \theta_e \le \dfrac{168\pi}{180} \\[2mm] \dfrac{-8}{15}N_c & \dfrac{168\pi}{180} \le \theta_e \le \dfrac{192}{180\pi} \\[2mm] \dfrac{-23}{15}N_c & \dfrac{192\pi}{180} \le \theta_e \le \dfrac{336\pi}{180} \\[2mm] \dfrac{-8}{15}N_c & \dfrac{336\pi}{180} \le \theta_e \le 2\pi \end{cases} \tag{2.31}$$

For five phase winding the winding functions are $N_a(\theta_e)$, $N_b(\theta_e)$, $N_c(\theta_e)$, $N_d(\theta_e)$ and $N_e(\theta_e)$ for phases A, B, C, D, and E respectively.

This can be represented as

$$N_a(\theta_e) = \sum_{h=1,2,3..}^{\infty} A_h \cosh(\theta_e - \theta_{wd})$$

$$N_b(\theta e) = \sum_{h=1,2,3..}^{\infty} A_h \cosh(\theta_e - \theta_{wd} - \frac{2\pi}{5})$$

$$N_c(\theta e) = \sum_{h=1,2,3..}^{\infty} A_h \cosh(\theta_e - \theta_{wd} - \frac{4\pi}{5})$$

$$N_d(\theta e) = \sum_{h=1,2,3..}^{\infty} A_h \cosh(\theta_e - \theta_{wd} - \frac{6\pi}{5})$$

$$N_e(\theta e) = \sum_{h=1,2,3..}^{\infty} A_h \cosh(\theta_e - \theta_{wd} - \frac{8\pi}{5})$$

(2.32)

Where

$$A_h = \frac{2N_c}{\pi h}[2\sinh(\frac{7\pi}{15}) + \sinh(\frac{9\pi}{15})]$$

(2.33)

$$\theta_{wd} = \frac{7\pi}{15}$$

(2.34)

Phase current are $I_a(w_e t)$, $I_b(w_e t)$, $I_c(w_e t)$, $I_d(w_e t)$ and $I_e(w_e t)$ for phases A, B, C, D and E, respectively. This can be represented as

$$I_a(\omega_e t) = \sum_{k=1,3,7..}^{\infty} I_k \cos k(\omega_e t - \theta_d)$$

$$I_b(\omega_e t) = \sum_{k=1,3,7..}^{\infty} I_k \cos k(\omega_e t - \theta_d - \frac{2\pi}{5})$$

$$I_c(\omega_e t) = \sum_{k=1,3,7..}^{\infty} I_k \cos k(\omega_e t - \theta_d - \frac{4\pi}{5})$$

$$I_d(\omega_e t) = \sum_{k=1,3,7..}^{\infty} I_k \cos k(\omega_e t - \theta_d - \frac{6\pi}{5})$$

$$I_e(\omega_e t) = \sum_{k=1,3,7..}^{\infty} I_k \cos k(\omega_e t - \theta_d - \frac{8\pi}{5})$$

(2.35)

Magnetically Coupled Dual Stator Five Phase Permanent Magnet Synchronous Generator for Wind Power Application

Where I_k is the peak current and θ_d is the phase shift between the voltage and current.

MMF due to five phase winding (F_{ar}) can be calculated as

$$F_{ar}(\theta_e, \omega_e t) = N_a(\theta_e)Ia(\omega_e t) + N_b(\theta_e)I_b(\omega_e t)$$
$$+N_c(\theta_e)I_c(\omega_e t) + N_d(\theta_e)I_d(\omega_e t) + N_e(\theta_e)I_e(\omega_e t) \tag{2.36}$$

From the above equation, MMF due to five phase winding (F_{ar}) can be written as

$$F_{ar}(\theta_e, \omega_e t) = \sum_{h=1,2,3..}^{\infty} \sum_{k=1,3,7,....}^{\infty} \frac{A_h I_k}{2}[(1+4*(-1)^{h+k}\cos(h+k)\frac{2\pi}{5}\cos(h+k)\frac{\pi}{5})(\cos(h\theta_e + k\omega_e t - h\theta_{wd} - k\theta_d))$$
$$+(1+4*(-1)^{h-k}\cos(h-k)\frac{2\pi}{5}\cos(h-k)\frac{\pi}{5})(\cos(h\theta_e - k\omega_e t - h\theta_{wd} + k\theta_d))] \tag{2.37}$$

MMF due to five phase winding (F_{ar}) can be rewritten as

$$F_{ar}(\theta_e, \omega_e t) = \sum_{h=1,2,3..}^{\infty} \sum_{k=1,3,7..}^{\infty} F_{ar(h\pm k)}\cos(h\theta_e \pm k\omega_e t - h\theta_{wd} \mp k\theta_d) \tag{2.38}$$

MMF due to armature reaction (F_w) in the network can be given as

$$F_w = \frac{\sum_{h=1,2,3..}^{\infty} \sum_{k=1,3,7..}^{\infty} F_{ar(h\pm k)}}{2} \tag{2.39}$$

2.7.7. Flux and Magnetic Field Density due to Armature Reaction

The flux due to armature reaction can be found out using the IMC model shown in Fig. 2.12. This network has only five-phase winding MMF sources and reluctance of various parts of the machine. The air-gap flux (φ_{gar}) due to armature reaction can be given as

$$\varphi_{gar} = \frac{4F_w(R_{pm}R_H + 4R_{sl}\beta\gamma(1 + 2\alpha)R_r)}{R_{pm}R_G + R_D(R_{pm}R_H + 4R_{sl}\beta\gamma(1 + 2\alpha)R_r)} \tag{2.40}$$

where

$$R_G = (1 + 2\alpha)(R_{pm}4R_{sl} + R_{pm}R_r + 4R_{sl}R_r) + 4R_{pm}(R_{pm} + 4R_{sl}\gamma) \qquad (2.41)$$

$$R_H = (1 + 2\alpha)(2R_{pm} + \gamma R_r + \beta(R_{sl} + R_r)) + 4R_{pm}(\gamma + \beta) + 16\beta\gamma R_{sl} \qquad (2.42)$$

Using Eq. 40, Flux density (B_{ar}) in the air-gap due to armature reaction can be found out.

2.8.   Finite Element Method Model for SSFP-PMSG

The predicted electromagnetic performances of the analytically designed model are validated with the finite element method (FEM) results because of high accuracy. For the electromagnetic analysis, basically, three analysis are commonly used namely magnetostatic, harmonic and transient. For this analysis, the four steps need to performed namely modeling, meshing, solution and post-processing. The modeling is done according to the specification presented in Table 2.5 for the SSFP-PMSG and schematic given in Fig. 2.7. Before the electromagnetic solution, the meshing of the model is required. The number of meshing element effect the accuracy of the model. After the solution, the results are found in post-processing steps. In the magnetostatic analysis, the rotor is fixed and the magnetic field solution can be found out at the fixed position of the rotor. The accuracy of the results gets better using transient analysis because the movement of the rotor is taken into account. There are two MMF sources present in the model namely stator winding and the permanent magnets of the rotor. The flux line due to four pair of magnetic poles confirms the eight poles of SSFP-PMSG as shown in Fig. 2.17. As the rotor rotates at rated speed of 400 rpm, the generator starts to generate the voltage at the frequency of 26.667 Hz. When the

generator is loaded, the five-phase current is drawn by the balanced load. Due to the armature MMF, the 8 poles are created which is shown in fig. 2.18.
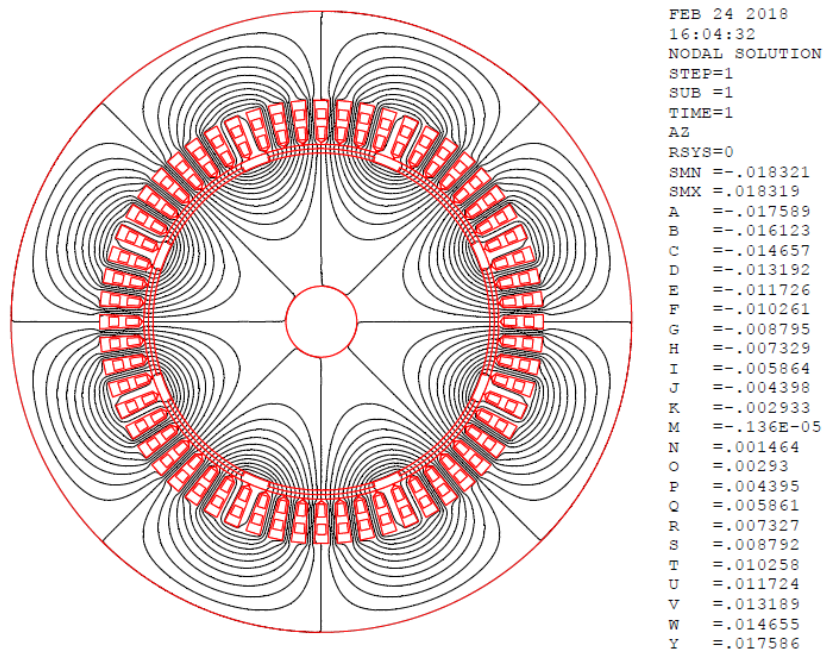


```
FEB 24 2018
16:04:32
NODAL SOLUTION
STEP=1
SUB =1
TIME=1
AZ
RSYS=0
SMN =-.018321
SMX =.018319
A   =-.017589
B   =-.016123
C   =-.014657
D   =-.013192
E   =-.011726
F   =-.010261
G   =-.008795
H   =-.007329
I   =-.005864
J   =-.004398
K   =-.002933
M   =-.136E-05
N   =.001464
O   =.00293
P   =.004395
Q   =.005861
R   =.007327
S   =.008792
T   =.010258
U   =.011724
V   =.013189
W   =.014655
Y   =.017586
```

Fig. 2.17 Flux lines plot due to four pair of rotor PMs of SSFP-PMSG

.


```
FEB 26 2018
19:45:45
NODAL SOLUTION
STEP=1
SUB =1
FREQ=26.667
REAL ONLY
AZ
RSYS=0
SMN =-.009335
SMX =.009335
    -.008989
    -.008297
    -.007606
    -.006915
    -.006223
    -.00484
    -.004149
    -.003457
    -.002766
    -.001383
    -.691E-03
    -.309E-07
    .691E-03
    .002074
    .002766
    .003457
    .004149
    .005532
    .006223
    .006915
    .007606
    .008989
```
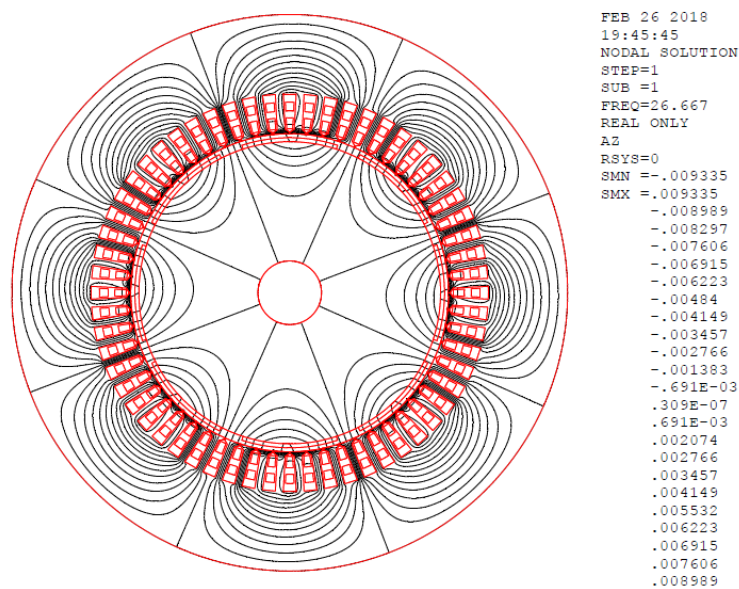
Fig. 2.18 Flux lines plot due to MMF of five Phase winding of SSFP-PMSG

The generator is designed such that the stator and rotor core should not be saturated with the combined effect of the fluxes from these two MMF sources. The flux due the armature winding depends on the nature of load due to which it either supports or opposes the PM fluxes. Fig. 2.19 and Fig. 2.20 show that the peak flux density due to PMs and stator winding are around 1.45 Tesla and 0.10 Tesla, respectively. It confirms that the combined effects of the two flux densities is lesser than the peak saturated value 1.8 Tesla in the stator teeth.

The magnetic flux distribution confirms the model accuracy which is the building block for the other performances like cogging torque, generated phase voltage, computation of inductances, electromagnetic torque etc;
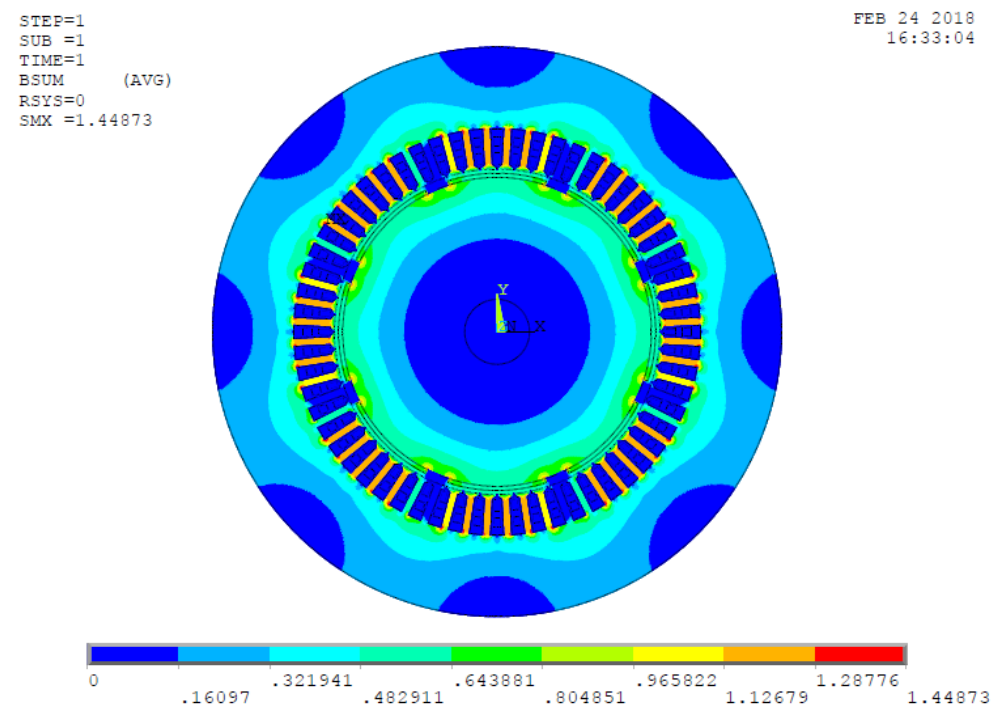

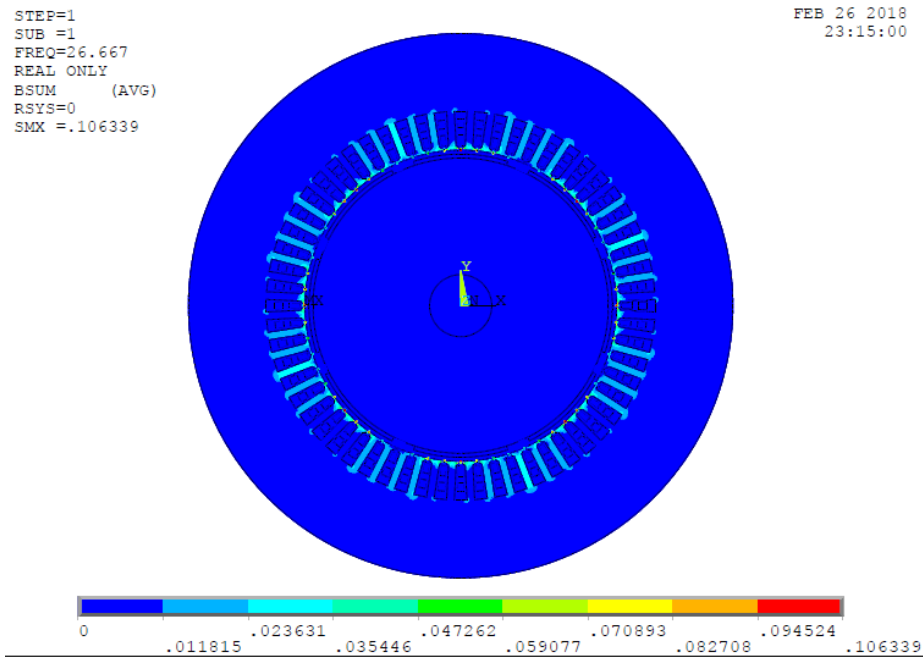Fig. 2.19 Flux density plot due to rotor PMs of SSFP-PMSG

.

```
STEP=1                                                    FEB 26 2018
SUB =1                                                      23:15:00
FREQ=26.667
REAL ONLY
BSUM      (AVG)
RSYS=0
SMX =.106339
```

| 0 | .011815 | .023631 | .035446 | .047262 | .059077 | .070893 | .082708 | .094524 | .106339 |

Fig. 2.20 Flux density plot due to winding MMF of SSFP-PMSG

2.9. Results and Model Verification

The flux distribution in the air-gap depends on the dimensional parameters, material properties, and armature reaction. The armature reaction flux has less significance than PMs flux so the design optimization is carried out under no-load condition. The dimensions which directly affect flux distribution include the height of magnet, magnet to magnet gap and width of rotor sleeve. For optimum magnet design, it is required to vary these parameters keeping the dimensions fixed for the machine. In addition, proper selection of material eliminates the non-linear behavior of core and also reduces the space harmonics. For this, different core and rotor sleeve material are considered to realize their effect on the distribution of air-gap flux. Furthermore, steel M400-50A is also considered for the realization of the adverse effect of saturation. In this context, IMC is proposed which calculates the distribution of air-gap flux density. Equations (2.23) and (2.24) are used to compute the magnetic flux density in air-gap

and surface of the magnet under no-load, respectively. Equations (2.27) and (2.29) present the effect on generated voltage and cogging torque. Under loading condition, the effect of armature reaction on air-gap magnetic flux density and performance is also carried out. The analytical results of IMC are verified with FEM results in the following Section.

2.9.1. Variation of Stator and Rotor Core Material

The flux distribution is directly associated with the core material as shown in Table 2.9. It is found that as the core material varies from air to amorphous steel, the air-gap flux density is increased by 118.177%. Similarly, for Cast iron and Silicon steel, it is increased to 115.67% and 118.15% with respect to air. The FEM for Bg is higher than analytical by 2.443%. As compared to air core the flux density at the surface of the magnet is increased by 100.3%, 98.179% and 100.286% for amorphous steel, Cast iron, and Silicon steel, respectively. The FEM result for Bm is higher by 2.029% to that of analytical results. Among these materials, amorphous steel has maximum Bg and Bm because of high permeability. It has lower conductivity and hence reduced iron loss.

Table 2.9: Variation of stator and rotor core material

Parameter	Analytical		FEM	
Core Materials	B_g (T)	B_m (T)	B_g (T)	B_m (T)
Silicon steel alloy	0.562070	0.637982	0.569370	0.645280
Cast iron	0.555677	0.631270	0.563000	0.638400
Air	0.257648	0.318535	0.264100	0.325000
Amorphous	0.562129	0.638039	0.569430	0.645340

steel alloy				

2.9.2. Variation of Rotor Sleeve Material

The variation of rotor sleeve material is enlisted in Table 2.10. It is observed that there is no variation in the air-gap flux density and the flux density at the surface of permanent magnets because of non-magnetic rotor sleeve-Al, copper, carbon fiber. However, for Al, the FEM results of B_g and B_m are found to be respectively, 1.302% and 1.144% higher than predicted results. For stainless steel, the B_g and B_m are increased by 4.47% and 3.923%, respectively. Among these materials, magnetic silicon steel has maximum B_g and B_m because of high permeability, but it provides the lowest reluctance path for leakage flux which enhances the local fluxes in the PMs, leads to demagnetization effect in it. Because of that it is avoided in general practice as a sleeve. The carbon fibre is an attractive solution with lower conductivity but occupies larger rotor volume.

Table 2.10: Variation of rotor sleeve material

Parameter	Analytical		FEM	
Rotor sleeve material	B_g (T)	B_m (T)	B_g (T)	B_m (T)
Stainless steel	0.585818	0.663014	0.592518	0.669700
Al	0.562075	0.637982	0.569375	0.645280
Copper	0.562075	0.637982	0.569375	0.645280
Carbon fiber	0.562075	0.637982	0.569375	0.645280

2.9.3. Variation of Height of Permanent Magnet

For this analysis, M400-50A steel alloy is used as the core and Al with 0.2 mm width is used as rotor sleeve. The magnet to magnet gap is 9° and inner and outer radius of stator and rotor are kept fixed. As height of the magnet is increased the air-gap length decreases, due to which air-gap flux enhances. The permeability of actual machine varies with saturation of core material and stator teeth are the most sensitive part with respect to saturation. From Table 2.11 the height of magnet varies from 1 mm to 2.5 mm, the B_g and B_m are increased linearly by 152.97 % and 121.91 %, respectively with respect to 1 mm magnet. Further, non-linearity creeps in as a consequence of saturation of stator teeth, as the height of magnet is increased from 2.5 to 3.5 mm in case of NdFeB and the maximum air-gap flux density is found to be 0.6585 Tesla (T) at 3.5 mm. As we go beyond 3.5 mm to 4.5 mm, flux density starts to decrease in the air-gap. The analytical and FEM results for NdFeB are verified and are found to be in close agreement. Since the generated voltage and the cogging torque are directly associated with the air-gap flux so a similar effect is found due to saturation, which are shown in Fig. 2.21 and Fig. 2.22 respectively. Similarly, Fig. 2.23 shows better visualization of adverse effect of saturation on the no-load performance under varying PM dimensions. It also shows that the FEM and analytical results are in good agreement under saturation condition because their material properties are taken care.

Table 2.11: Variation of permanent magnet height

Parameter		Analytical		FEM	
H_{pm} (mm)	g_e (mm)	B_g (T)	B_m (T)	B_g (T)	B_m (T)
1.0	3.8	0.22222	0.28750	0.22510	0.29370
1.5	3.3	0.33310	0.40920	0.33670	0.41560

2.0	2.8	0.44490	0.52490	0.45050	0.53120
2.5	2.3	0.56210	0.63800	0.56940	0.64530
3.0	1.8	0.63500	0.71223	0.64320	0.71945
3.5	1.3	0.65850	0.73675	0.66690	0.74621
4.0	0.8	0.65680	0.72940	0.66540	0.73889
4.5	0.3	0.61510	0.69039	0.62290	0.69748

2.9.4. Variation of Rotor Aluminium Sleeve Thickness

The flux density is affected by rotor sleeve thickness as shown in Table 2.12. For this analysis, the core is silicon steel, the height of the magnet is 2.5 mm and magnet to magnet gap is 9°. The dimensional parameter of the inner and outer radius of stator and rotor are also kept fixed. As the width of sleeve thickness varies from 0.1 mm to 1.0 mm,
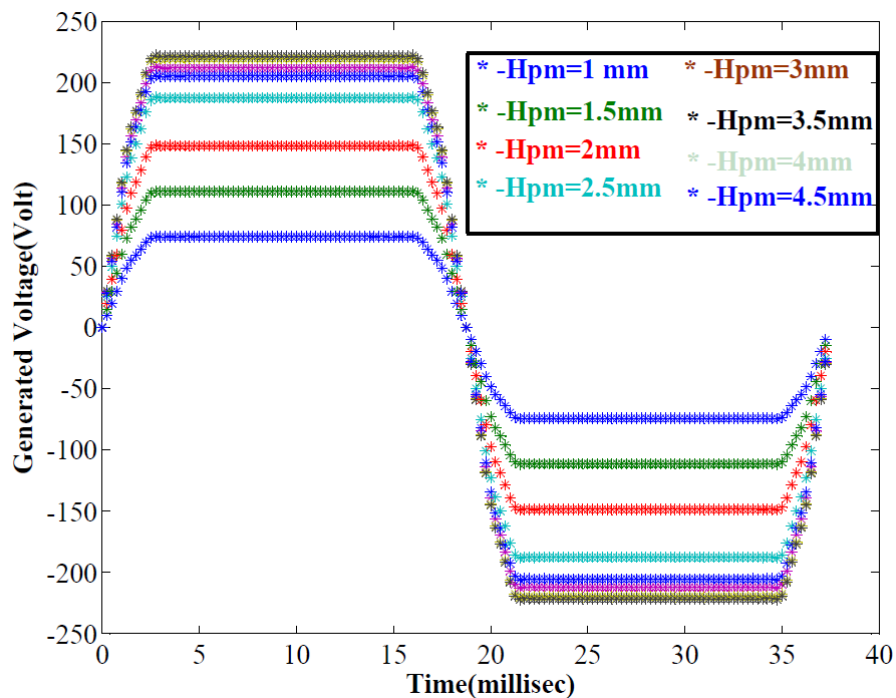
Fig. 2.21 Generated voltage due to variation of magnet height (1 mm to 4.5 mm)
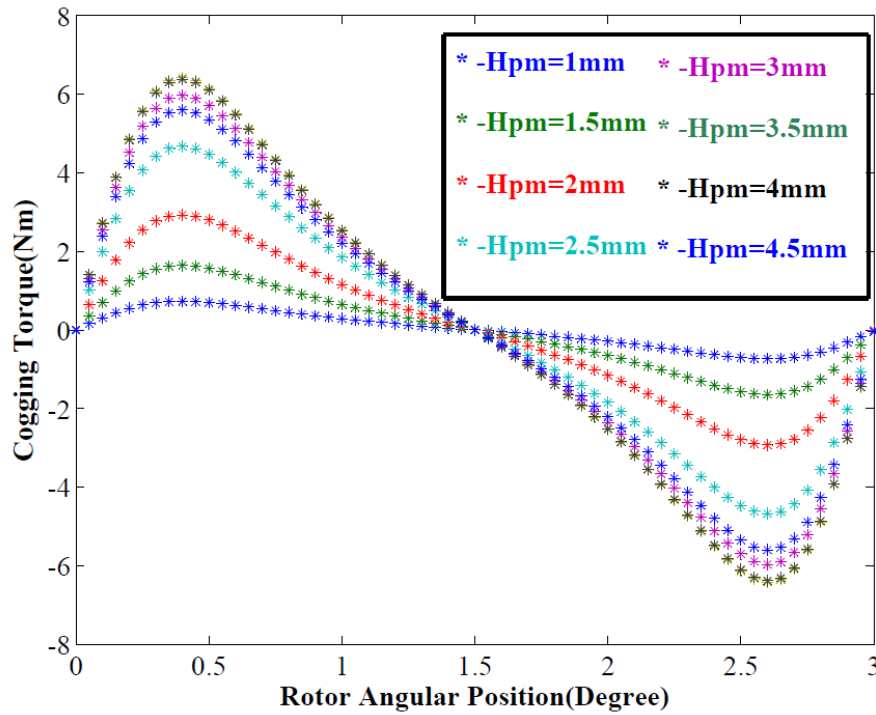
Fig 2.22 Cogging torque due to variation of magnet height (1 mm to 4.5 mm)
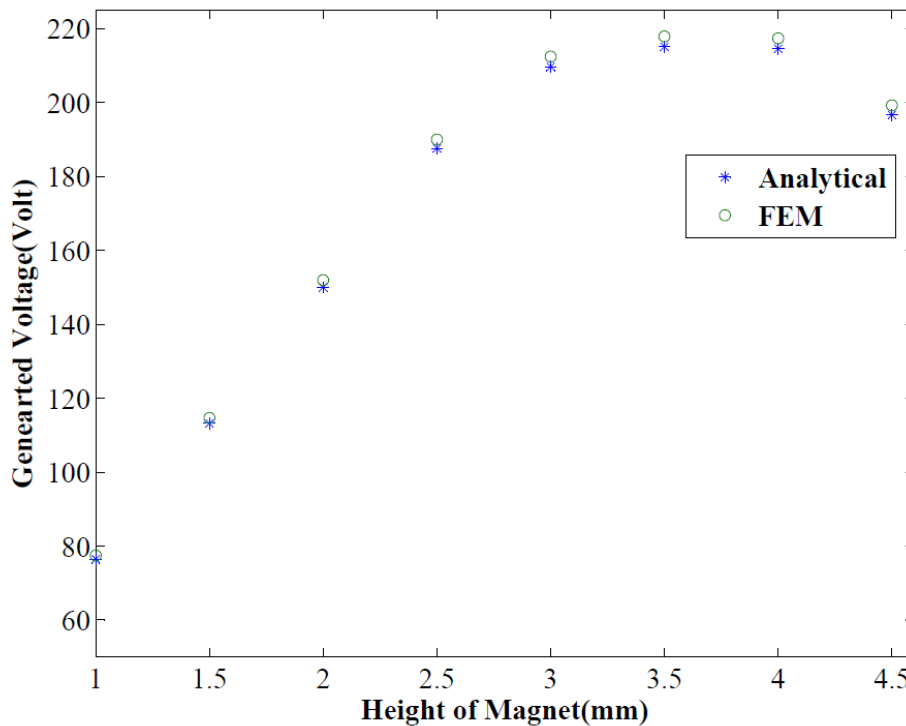
Fig 2.23 Generated Voltage with saturation due to variation of magnet height

Table 2.12: Variation of rotor sleeve thickness

Parameter		Analytical		FEM	
l_{sl} (mm)	g_e (mm)	B_g (T)	B_m (T)	B_g (T)	B_m (T)
0.1	2.4	0.5608	0.6397	0.5673	0.6466
0.2	2.3	0.5621	0.6380	0.5680	0.6450
0.3	2.2	0.5634	0.6363	0.5740	0.6427
0.4	2.1	0.5647	0.6348	0.5710	0.6416
0.5	2.0	0.5660	0.6333	0.5720	0.6400
0.6	1.9	0.5673	0.6318	0.5749	0.6383
0.7	1.8	0.5687	0.6304	0.5758	0.6373
0.8	1.7	0.5700	0.6290	0.5763	0.6351
0.9	1.6	0.5714	0.6277	0.5782	0.6233
1.0	1.5	0.5728	0.6264	0.5787	0.6335

the B_g is increased by 2.14% and the B_m is decreased by 2.079%. The simulated FEM results for B_g and B_m for 0.1 mm of sleeve thickness are 1.159% and 1.078% higher than predicted results. In this context, the generated voltage is increased by 2.191% as shown in Fig. 2.24. The cogging torque is also increased upto 4.343% due to the variation of rotor sleeve thickness as shown in Fig. 2.25.
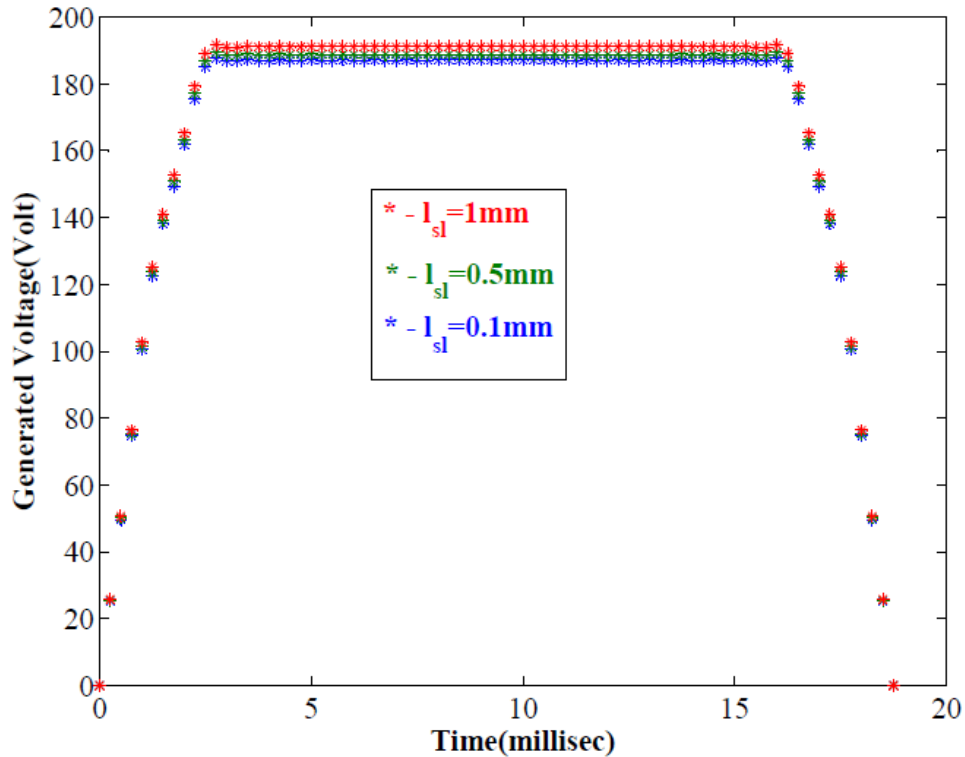
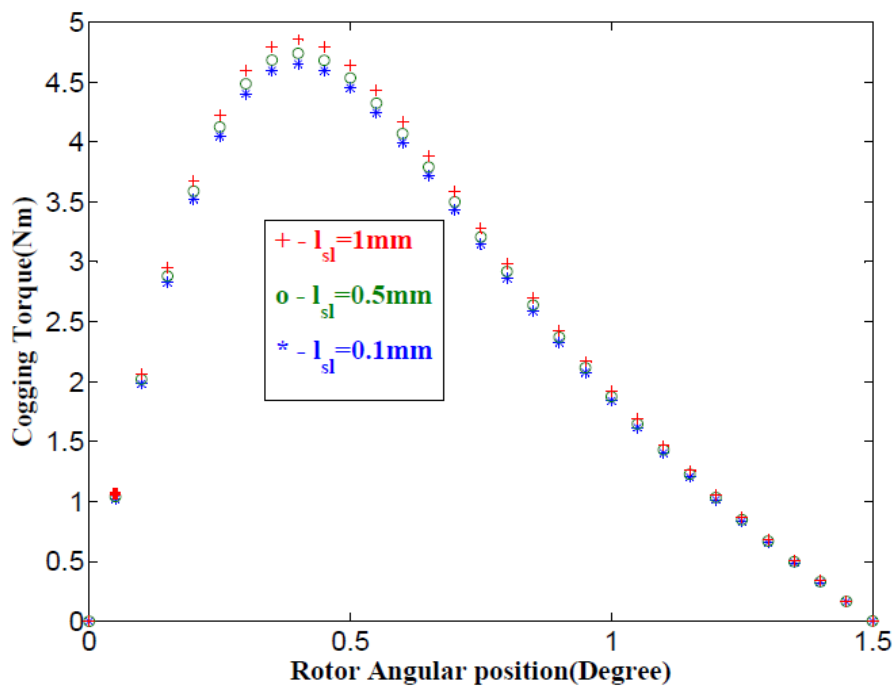Fig. 2.24 Generated Voltage with the Variation of rotor sleeve thickness (0.1 mm to 1 mm)

Fig 2.25 Cogging torque with the Variation of rotor sleeve thickness (0.1 mm to 1 mm)

2.9.5. Variation of Magnet to Magnet Gap

The distribution of flux is slightly affected by the magnet to magnet gap as given in Table 2.13. For this analysis, the core made of silicon steel alloy and Al sleeve with 0.2 mm is used. The height of the magnet is 2.5 mm and inner and outer radius of stator and rotor remains unchanged.

As the magnet to magnet gap increases, the flux in the air-gap decreases. The magnet to magnet gap is varied from 5.105 mm to 15.32 mm. It is observed that the Bg and Bm are decreased by 393.65% and increased by 285.739%, respectively. The simulated FEM results for B_g and B_m for 5.105 mm of magnet to magnet gap are 0.972% and 0.967% higher than calculated results. The generated voltage is decreased by upto 6.13% as shown in Fig. 2.26. On the other side cogging torque is decreased by 12.69% as presented in Fig. 2.27.

Table 2.13: Variation of arcilier length of permanent magnet

Parameter	Analytical		FEM	
δ (mm)	B_g (T)	B_m (T)	B_g (T)	B_m (T)
5.105	0.5967	0.5996	0.6025	0.6054
6.807	0.5949	0.6021	0.6013	0.6077
8.508	0.5893	0.6084	0.5951	0.6148
10.21	0.5831	0.6151	0.5887	0.6215
11.91	0.5765	0.6224	0.5825	0.6282
13.61	0.5695	0.6300	0.5759	0.6368
15.32	0.5621	0.6380	0.5694	0.6453

2.9.6. Impact of Armature Reaction on Magnetic Field Distribution

The effective value of air-gap flux (φ_{ge}) can be computed using IMC shown in Fig. 2.10. Since this network consists of two MMF sources hence the air-gap flux is the resultant of no-load flux (φ_g) due to the permanent magnet of the rotor and the armature reaction flux (φ_{ar}) due to five-phase winding. The no-load flux and armature fluxes are computed using Eqn. (2.22) and Eqn. (40) respectively. The air-gap flux density at no-load is found 0.5621 Tesla whereas 0.0841 Tesla due to armature reaction. The flux densities are also carried out using FEM, the no-load flux density is found 0.5694 T whereas the 0.0839 T due to five phase winding. The analytical results are found in good agreement with FEM result.
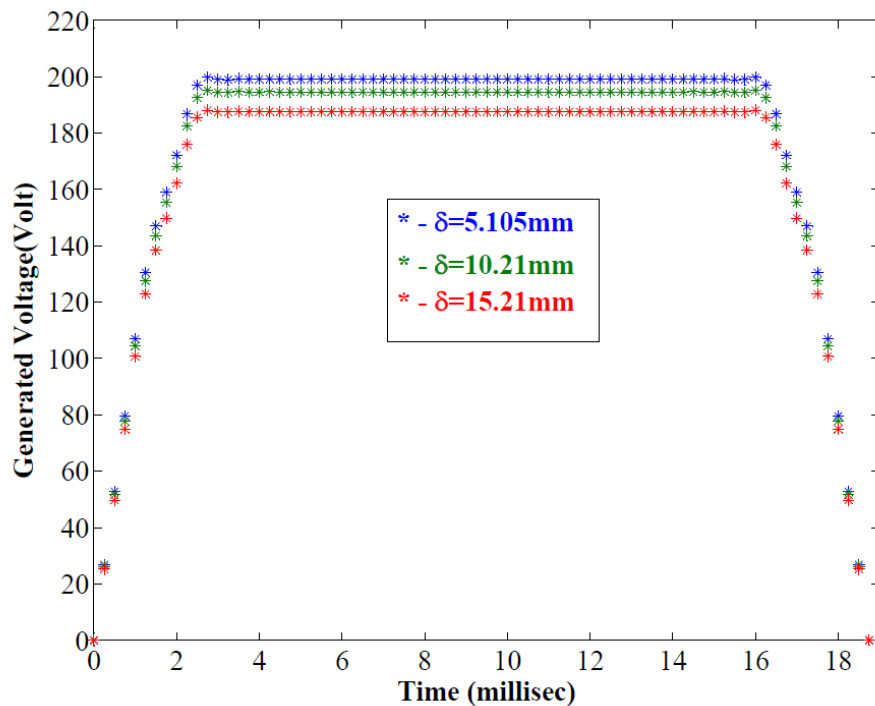
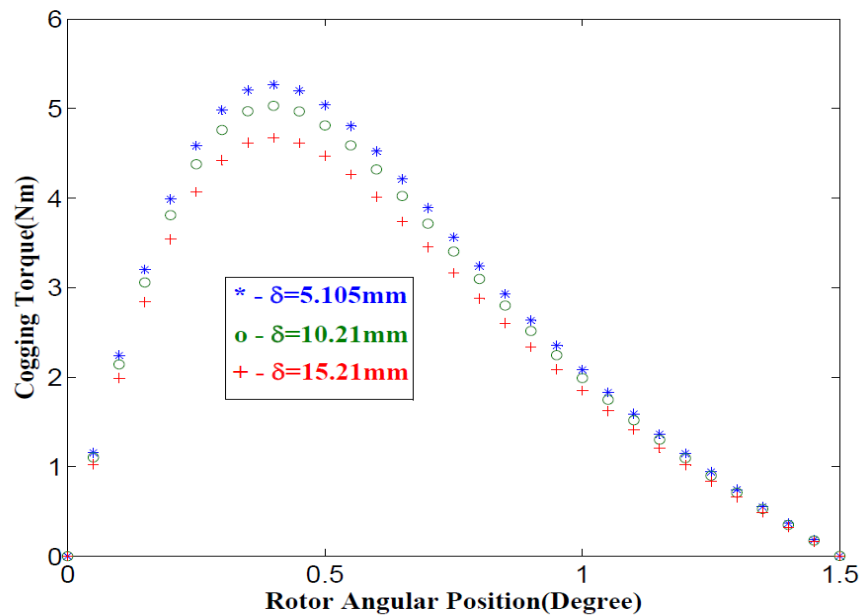Fig. 2.26 Generated Voltage with the variation of magnet to magnet gap (5.105 mm to 15.32 mm)

Fig. 2.27 Cogging torque with the variation of magnet to magnet gap (5.105 mm to 15.32mm)

2.10. IMC Model of Air-Gap Flux for MCDSFP-PMSG

As discussed in section 2.2, the dual stator annular rotor is having three possible flux paths- two are local leakage flux path and one is coupled flux paths shown in Fig. 2.1. To decrease the local leakage flux through the rotor has to be segmented as shown in Fig. 2.2. The rotor flux barrier width needs to be optimized to minimise the harmonic in generated voltage and leakage flux. This is decided by the separation angle (α) of the segmented rotor, optimized value of which is discussed in Section 2.11.

To compute the magnetic flux distribution and electromagnetic performances, an improved magnetic circuit model is developed for the MCDSFP-PMSG. The reluctance network model (RNM) is applied for the estimation of machine characteristics. The permeability of the magnetic material is assumed to be constant. Since 60 slots and 20 slots are having quarter periodicity for eight poles of the rotor, so the machine is modeled only for one-fourth of the model. Fig. 2.27 represents complete magnetic

circuit for the quarter model. It consists of reluctances of main flux path, flux barrier path and the sources of MMFs. The reluctances are of two types: one which is fixed with rotor position and can be calculated using existing formulae [145-147]; and another varies with rotor position that needs an interaction of teeth and PM [148], [149] for calculations.

The reluctance of inner or outer stator yoke

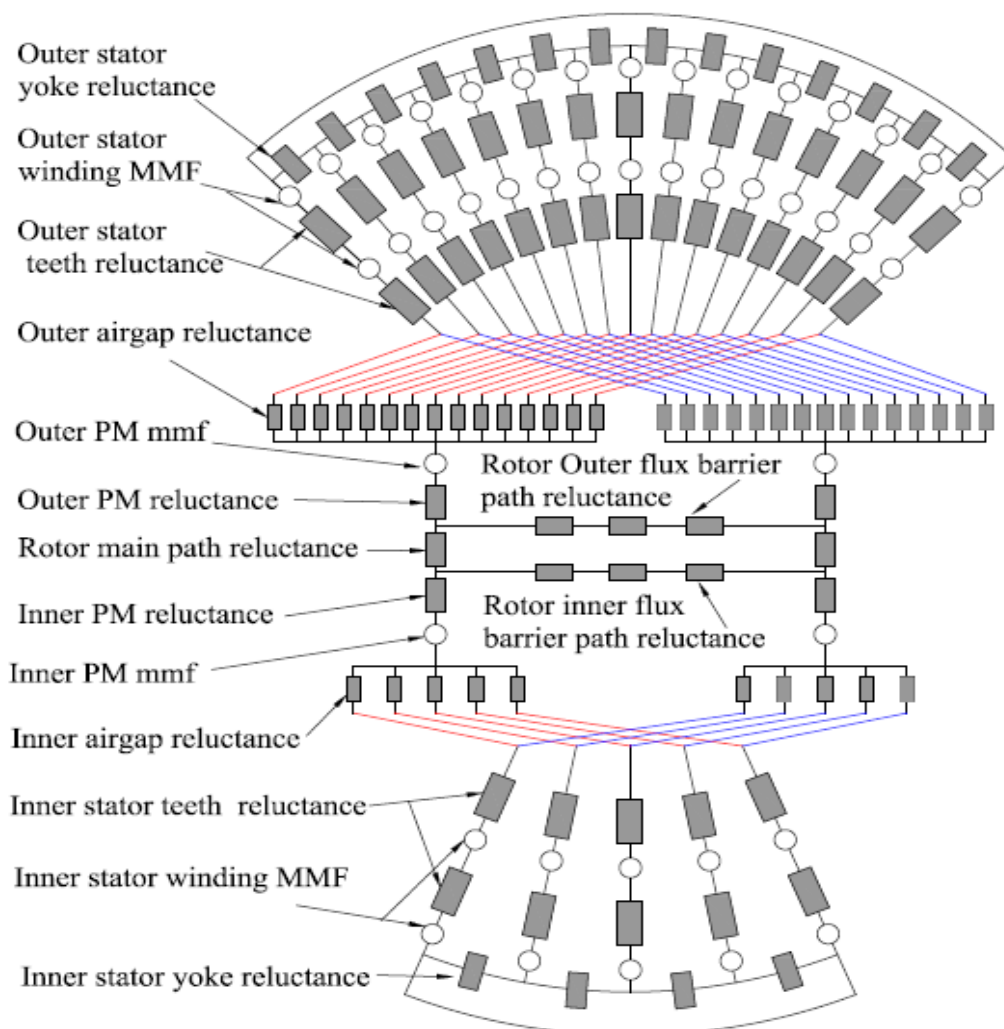$$R_{si,o} = \frac{l_{sy}}{2\pi\mu_o \mu_{fe} r_s \theta_p L_i}$$

(2.43)

Fig. 2.28 RNM of MCDSFP-PMSG

The reluctance of inner or outer stator tooth

$$R_{sti,o} = \frac{h_t}{\mu_o \mu_{fe} w_t L_i} \qquad (2.44)$$

The reluctance of permanent magnet

$$R_{pmi,o} = \frac{H_{pm}}{\mu_o \mu_{pm} l_m L} \qquad (2.45)$$

The reluctance of rotor yoke

$$R_r = \frac{l_{ry}}{2\pi \mu_o \mu_{fe} r_r \theta_p L_i} \qquad (2.46)$$

The reluctance of iron paths of flux barrier

$$R_{iri,o} = \frac{r_{rm} \dfrac{(\theta_p - \alpha)}{2}}{\mu_o \mu_{fe} \dfrac{l_{ry}}{2} L_i} \qquad (2.47)$$

The reluctance of air paths of flux barrier

$$R_{gri,o} = \frac{r_{rm} \alpha}{\mu_o \dfrac{l_{ry}}{2} L_i} \qquad (2.48)$$

where r_{rm} is the radius at the middle of upper and lower part of the rotor yoke.

Reluctance of air-gap

$$R_g = \frac{g_{eff}}{\mu_o . width . L} \qquad (2.49)$$

where width=$r_g \beta_{t-pm}$ and β_{t-pm} is the interaction angle between tooth and PM.

Using above equations, the computed fixed reluctances are enlisted in Table 2.14. The various air gap reluctances due to interaction of tooth and PM are calculated

corresponding to rotor position at t = 0 sec. These are enlisted in Table 2.15. For estimating the variable air-gap reluctances with respect to various rotor positions, computation was done using Eqn. (2.49) in steps of 0.1^OE (electrical). In total 3600 air-gap reluctance values where used to create Table 2.15 for different rotor positions. These reluctances and MMFs are substituted in the RNM for estimating mean air-gap flux density due to PM and armature winding MMFs, listed in Table 2.16.

Table 2.14: Fixed reluctances for MNCDSFP-PMSG

Reluctance	Symbol	Value (Ampere-turns/weber)
Inner magnet	R_{pmi}	$4.7583*10^5$
Outer magnet	R_{pmo}	$2.6463*10^5$
Inner stator yoke	R_{si}	162.9692
Outer stator yoke	R_{so}	301.3813
Rotor iron	R_r	143.0137
Iron of inner flux barrier	R_{iri}	$1.2591*10^3$
Iron of outer flux barrier	R_{iro}	$1.6905*10^3$
Air of inner flux barrier	R_{gri}	$1.3512*10^6$
Air of outer flux barrier	R_{gro}	$1.8142*10^6$

.

Table 2.15: Reluctances due to interaction of stator teeth and PM

Reluctance	Symbol	Value (Ampere-turns/weber)
Inner tooth1 and PM1	t_1-PM$_1$	$3.8476*10^6$
Inner tooth2 and PM1	t_2-PM$_1$	$1.0500*10^6$

Inner tooth3 and PM1	t_3-PM_1	$1.3585*10^6$
Inner tooth4 and PM1	t_4-PM_2	$1.3585*10^6$
Inner tooth5 and PM1	t_5-PM_2	$1.0500*10^6$
Inner tooth6 and PM1	t_6-PM_2	$3.8476*10^6$
Outer tooth2 and PM1	t_2-PM_1	$2.8095*10^6$
Outer tooth3 and PM1	$t3$-PM_1	$1.5391*10^6$
Outer tooth4 and PM1	t_4-PM_1	$1.5391*10^6$
Outer tooth5 and PM1	t_5-PM_1	$1.5391*10^6$
Outer tooth6 and PM1	t_6-PM_1	$1.5391*10^6$
Outer tooth7 and PM1	t_7-PM_1	$1.5391*10^6$
Outer tooth8 and PM1	t_8-PM_1	$3.2192*10^7$
Outer tooth9 and PM1	t_9-PM_2	$3.2192*10^7$
Outer tooth10 and PM1	t_{10}-PM_2	$1.5391*10^6$
Outer tooth11 and PM1	t_{11}-PM_2	$1.5391*10^6$
Outer tooth12 and PM1	t_{12}-PM_2	$1.5391*10^6$
Outer tooth13 and PM1	t_{13}-PM_2	$1.5391*10^6$
Outer tooth14 and PM1	t_{14}-PM_2	$1.5391*10^6$
Outer tooth15 and PM1	t_{15}-PM_2	$2.8095*10^6$

2.10.1. Design and Optimization of Proposed Novel Segmented Rotor Topology

The rotor is segmented into eight parts, which pushes the useful flux in a predefined path. The useful flux is created due to the magnetic coupling of inner and

outer rotor MMF sources. These two design features have been integrated into the IMC
Model. Fig. 2.29 shows IMC Model for MCDSFP-PMSG under one pole-pitch. It
consists of MMF sources and reluctances of various parts. In between the rotor
segments, either air or non-magnetic material may be filled. Here air is considered in
between the segments. To avoid leakage flux through the flux barrier path, the rotor
yoke is designed just to avoid the threshold of core saturation. Leakage fluxes of the
flux barrier path are φ_{ryi} and φ_{ryo} as shown in Fig. 2.29.
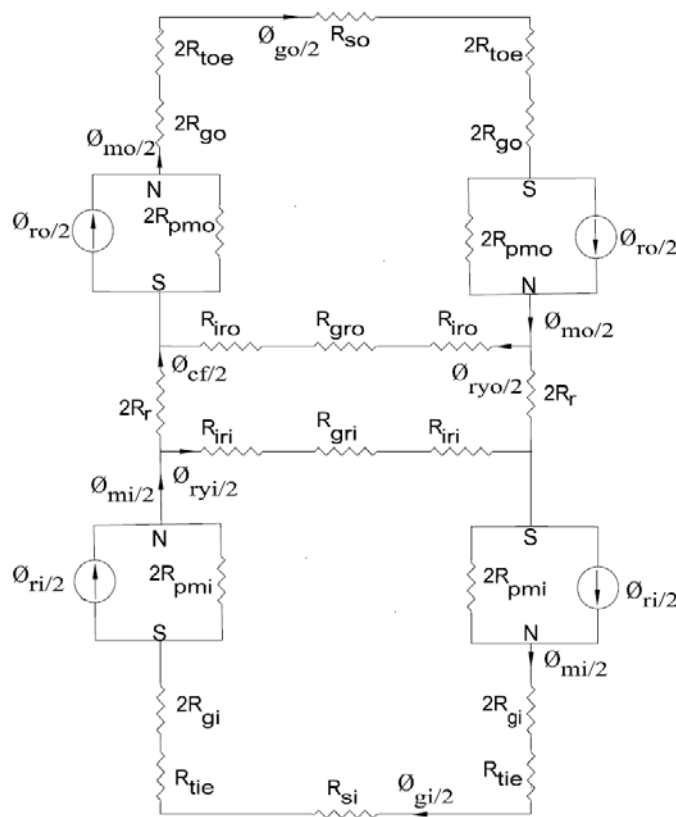
Fig. 2.29 IMC Model of MCDSFP-PMSG under one pole pitch

Leakage flux through inner portion of rotor

$$\frac{\varphi_{ryi}}{2} = \frac{2F_i(r_1r_2 + 4R_r(r_1 + r_2)) - 2F_o r_2 r_4}{r_1r_2(r_3 + r_4) + (r_3r_4 + 4R_r(r_3 + r_4))(r_1 + r_2)} \qquad (2.50)$$

Leakage flux through outer portion of rotor

$$\frac{\varphi_{ryo}}{2} = \frac{2F_o(r_3 r_4 + 4R_r(r_3 + r_4)) - 2F_i r_1 r_3}{r_1 r_2 (r_3 + r_4) + (r_3 r_4 + 4R_r(r_3 + r_4))(r_1 + r_2)} \qquad (2.51)$$

where,

$$r_1 = 4R_{pmo} + 4R_{go} + R_{so} + 2R_{toe} \qquad (2.52)$$

$$r_2 = 2R_{iro} + R_{gro} \qquad (2.53)$$

$$r_3 = 2R_{iri} + R_{gri} \qquad (2.54)$$

$$r_4 = 4R_{pmi} + 4R_{gi} + R_{si} + 2R_{tie} \qquad (2.55)$$

Though leakage flux through the local path is approximately 0.978 mWb for unsegmented rotor, it reduces significantly with the increase in separation angle (α) between the segments. Positive and negative flux leakage implies relative bipolar nature of flux. Fig. 30 suggests that leakage flux primarily varies from 0° to 9°. However, it becomes less significant after $\alpha=4^o$. For $\alpha> 4^o$, harmonics would start appearing in the air-gap magnetic flux density. Therefore, $\alpha=4^o$ is considered as the optimum design point corresponding to which the leakage flux is below 0.43 mWb.

2.10.2. EMF and Load Performance

The magnetic flux distribution in outer and inner air-gaps is flat-topped due to arc-shaped magnets. This results in odd harmonics components. The short pitching of magnets reduces the weight of magnets, which makes the machine cost effective. Eqn. (2.56) and Eqn. (2.57) show magnetic flux distribution of outer and inner air-gaps, respectively.
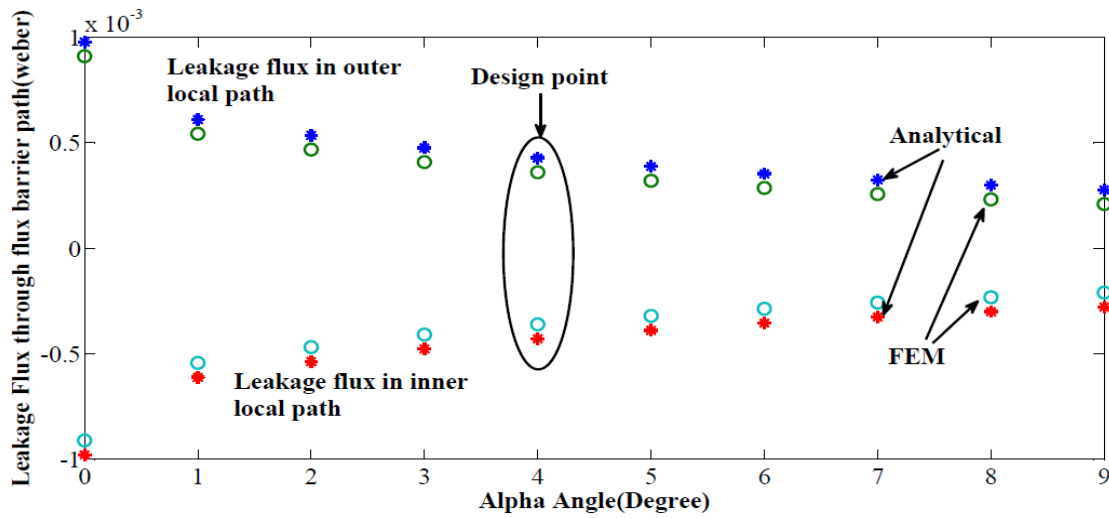
Fig. 2.30 Leakage flux variation through flux barrier with α

Magnetic flux density due to PM's in the Outer air-gap

$$B_o(\theta_{er}) = \sum_{k=1,3,5}^{\infty} B_{gmko} sin(k\theta_{er}) \qquad (2.56)$$

Magnetic flux density due to PM's in the Inner air-gap

$$B_i(\theta_{er}) = \sum_{k=1.3.5}^{\infty} B_{gmki} \cdot sin(k\theta_{er}) \qquad (2.57)$$

where, for inner airgap mean flux density (B_{gmki}) and outer air-gap mean flux density (B_{gmko}), the peak value of corresponding flux densities are

$$B_{gmko} = \frac{4}{\pi(\frac{\pi}{2} - \beta)} \frac{B_{gmo}}{k^2} cos(k\beta) \, sin(k\frac{\pi}{2}) \qquad (2.58)$$

$$B_{gmki} = \frac{4}{\pi(\frac{\pi}{2} - \beta)} \frac{B_{gmi}}{k^2} cos(k\beta) \, sin(k\frac{\pi}{2}) \qquad (2.59)$$

The induced voltage in the Outer stator winding

$$E_o = \sum_{k=1,3,7}^{\infty} E_{oack} \sin(kw_e t) \tag{2.60}$$

where,

$$E_{oack} = \frac{8}{P'} \times 2.9563 \times N_{oc} L_i r_{so} w_e B_{gmko} \cos(k\frac{\pi}{30}) \tag{2.61}$$

The induced voltage in the inner stator winding

$$E_i = \sum_{k=1,3,7}^{\infty} E_{iack} \sin(k(w_e t - \frac{\pi}{15})) \tag{2.62}$$

where,

$$E_{iack} = \frac{8}{P'} N_{ic} L_i r_{si} w_e B_{gmki} \cos(k\frac{\pi}{10}) \tag{2.63}$$

$$THD = \frac{\sqrt{\sum_{k=3,7,9}^{\infty} E_{ack}^2}}{E_{ac1}} \tag{2.64}$$

Using Eqn. (2.64), the FFT analysis of generated EMF in inner and outer stator winding provide information about the amplitude and order of harmonics. Fig. 2.31 and Fig. 2.32 shows FFT for inner and outer stator generated EMF respectively. This confirms that multiple of 5th order harmonics are absent. The THD of outer EMF is 18.14% and inner EMF is 21.87%. The higher THD of inner stator EMF is due to concentrated nature of winding.

Due to per phase winding inductance and resistance, for purely resistive load connected to the generator, the terminal voltage at rated load (V_{Lo},i) lags behind the no-load voltage (E_o,i). This is because of the armature reaction and impedance drop (I_o,$_I Z_{pho}$,i) as per equation (2.65).

$$E_{o,i} = I_{o,i}Z_{pho,i} + V_{Lo,i} \qquad (2.65)$$

The total output power for phase A is the summation of power supplied by the inner and the outer stator

$$P_{o,i}(t) = \sum_{k=0,2,4}^{\infty} P_{ko} cos(k(w_e t + \Psi_o)) + 1 \sum_{k=0,2,4}^{\infty} P_{ki} cos(k(w_e t + \Psi_i)) \quad (2.66)$$

Where, o and i are the power phase angles that depend on the phase voltage and phase current of outer and inner stator windings, respectively. Basically, the power phase angle is the angle for the kth harmonic, between the kth harmonic reference voltage and a kth harmonic power component. The moving torque (T) is calculated using total power of inner and outer stator for j number of phases

$$T = T_{cogg} + \frac{\sum_{j=1}^{5} P_{o,i}(t)}{w_m} \qquad (2.67)$$

T$_{cogg}$ is the cogging torque which can be found out using Eqn. (2.29).

The ripple torque (%)

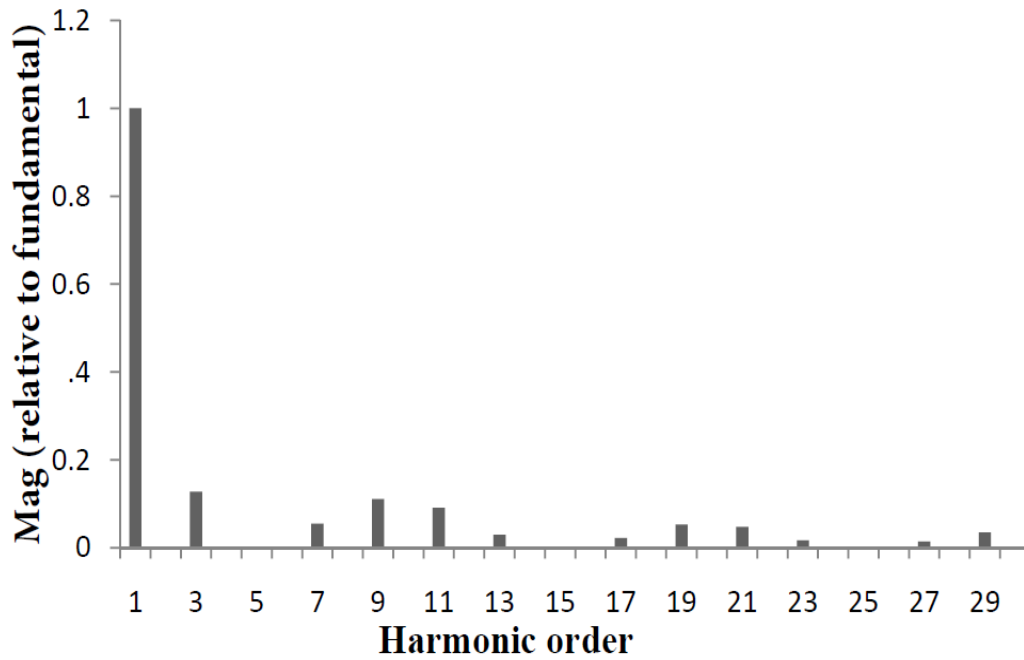$$T_{ripple} = \frac{T_{max} - T_{min}}{T_{average}} \times 100 \qquad (2.68)$$

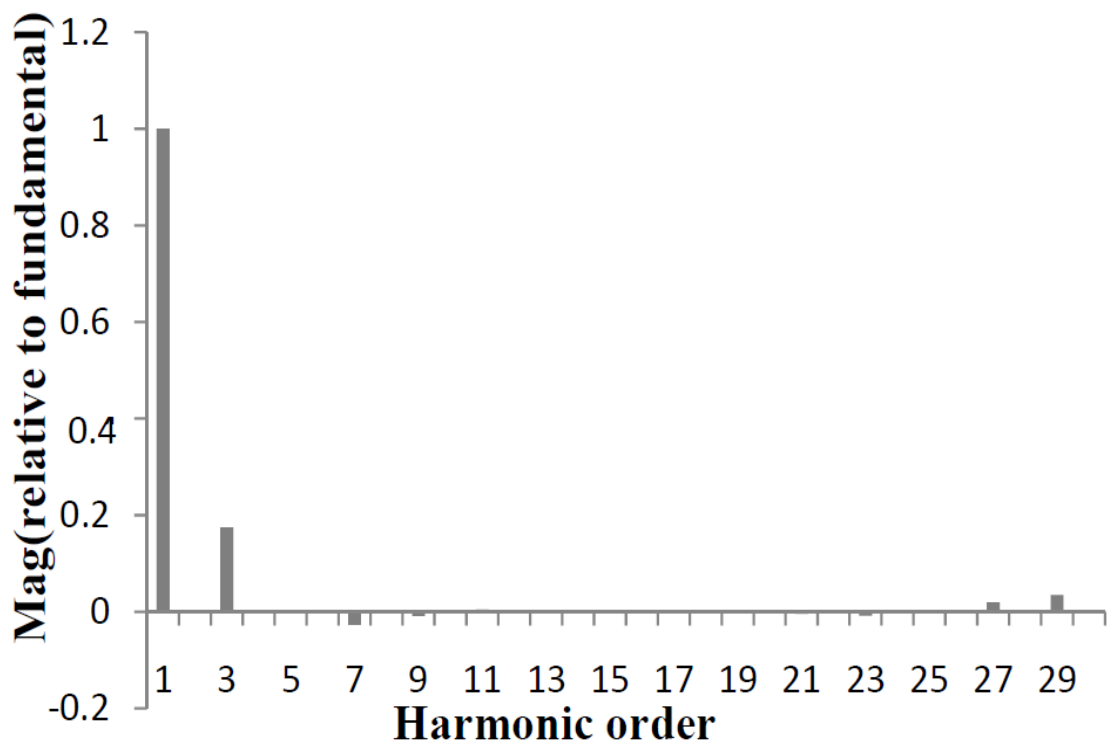Fig. 2.31 FFT analysis of No load inner stator EMF

Fig. 2.32 FFT analysis of No load outer stator EMF

2.11. FEM Analysis and Result Validation of MCDSFP-PMSG

The FEM simulation is performed using Ansoft Maxwell software. The 2D time-stepped finite-element analysis is carried out while the machine model is coupled with the external circuit. Meshing is triangular shaped with 36728 number of mesh elements. The external circuit, as shown in Fig.2.33, is required for evaluating the loading capability of the machine. With the possible winding inter connections; MCDSFP-PMSG can feed a wide range of load requirement besides the balanced standalone operation of inner and outer stator. Here external load on the generator is considered to be purely resistive. Due to a maximum percentage of current harmonics, it will provide the worst case scenario in terms of armature reaction. Although, as The per-phase self-inductance is 2.54 mH for inner and 43.36 mH for outer winding. The winding resistance is 1.015 ohm and 5.493 ohms for inner and outer windings, respectively. The external load resistance R_{Li} and R_{Lo} are decided by the magnitude of rated current. For rated current peak value of 4 A, R_{Li} =6.9914 ohms and R_{Lo} =47.40 ohms.

2.11.1. Magnetic Flux Distribution

The magnetic flux density using RNM is calculated along the main flux path for the midpoint of outer and inner air-gaps. These are compared with the FEM results, as shown in Fig. 2.34 and Fig. 2.35. The flux density using FEM and analytical method are reasonably close. The analytical result in the outer air-gap is 0.64% higher than FEM, whereas in the inner air-gap it is 0.732% higher than FEM.

2.11.2. MCDSFP-PMSG Characteristics

The analytical model generate EMFs at No-load for the outer, and the inner stator winding which is compared with FEM results as shown in Fig. 2.36 and Fig. 2.37. The results are in good agreement. The generated emf for the inner and the outer stator is trapezoidal. The inner stator phase voltage lags behind the outer stator voltage by 12°E as shown in Fig. 2.38. This difference is due to unequal coil spans. For inner stator winding coil, span is 144°E (electrical) while for the outer stator winding the coil span is 168°E (electrical). The generator is loaded using a resistive load. Due to resistive loading the terminal voltage magnitude is reduced by around 4.4 V and 36.4 V for the inner and the outer windings, respectively. The armature reaction and impedance drop are responsible for the drop in terminal voltage.

2.11.3. Machine Torque

The moving torque of the MCDSFP-PMSG is shown in Fig.2.39. The FEM result is 2.173% higher than the analytical. The ripple torque is due to the interaction of harmonics present in the flux density and armature current. It is 5.072% with FEM and 7.4% analytically. A comprehensive comparative table enlisting various analytical and FEM data are presented in Table 2.16.

Table 2.16: MCDSFP-PMSG performance parameters

Parameter	FEM	Analytical
Inner air-gap B-field (Tesla) due to PM	0.5695	0.5737
Outer air-gap B-field (Tesla) due to PM	0.5852	0.5890
Inner No-load phase voltage (Volts)	32.3679	32.3679
Outer No-load phase voltage (Volts)	226.02	227.4737

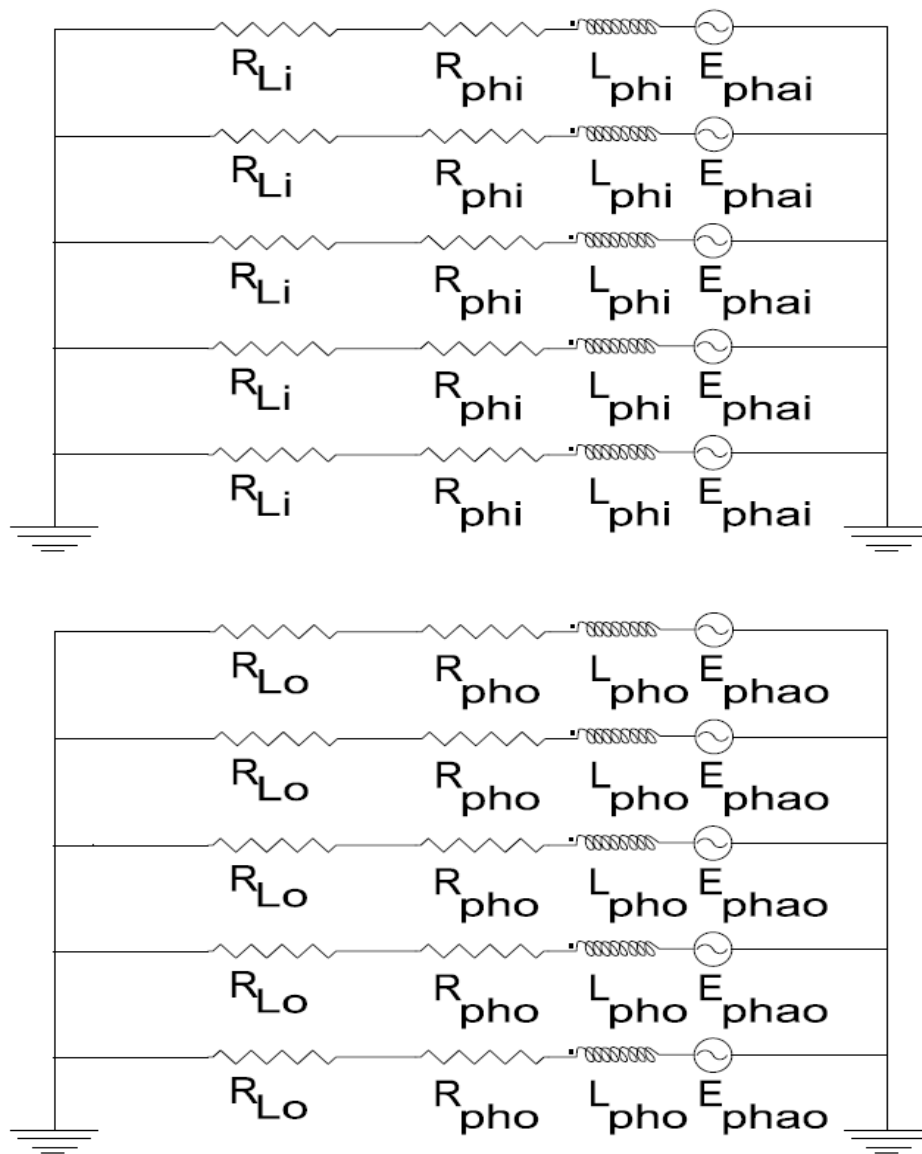|		
Inner induced Voltage at rated load(Volts)	27.965	27.966
Outer induced Voltage at rated load(Volts)	189.6	191.0
Moving torque at rated load (N.m)	110.4	108

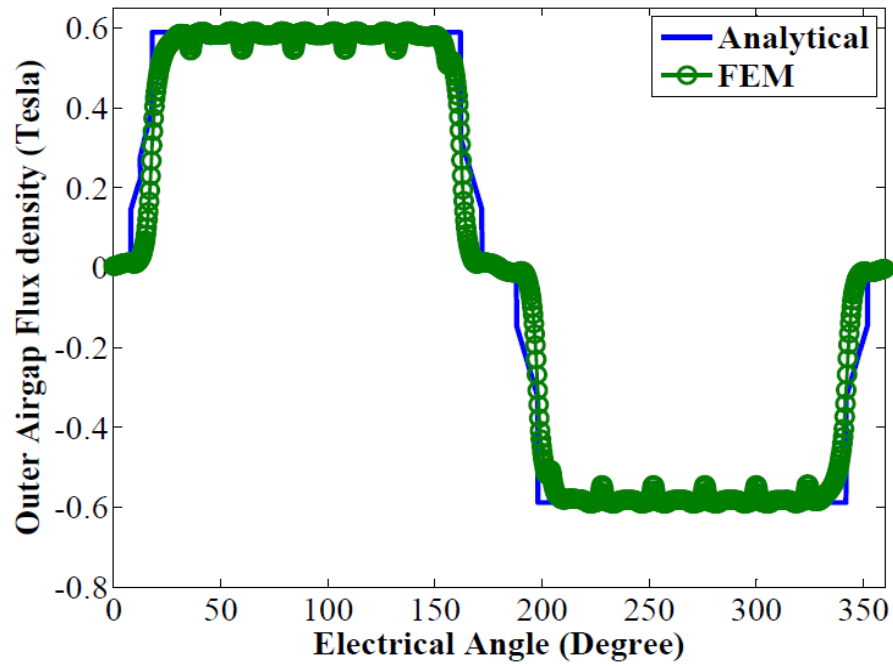Fig. 2.33 External circuit connected to MCDSFP-PMSG FEM model

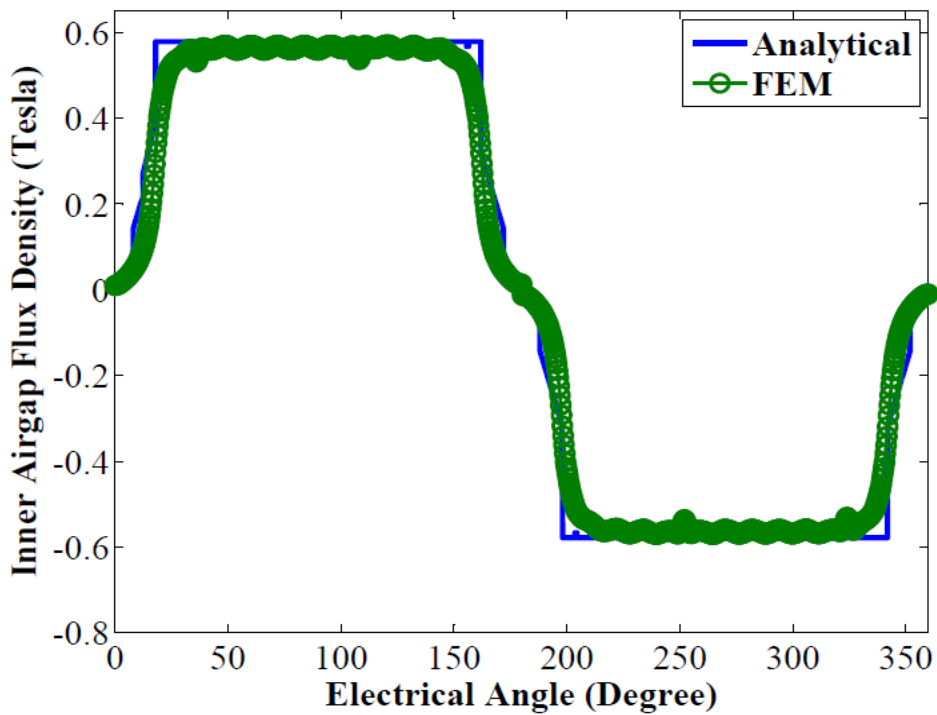Fig. 2.34 FEM and Analytical result of outer air gap flux density

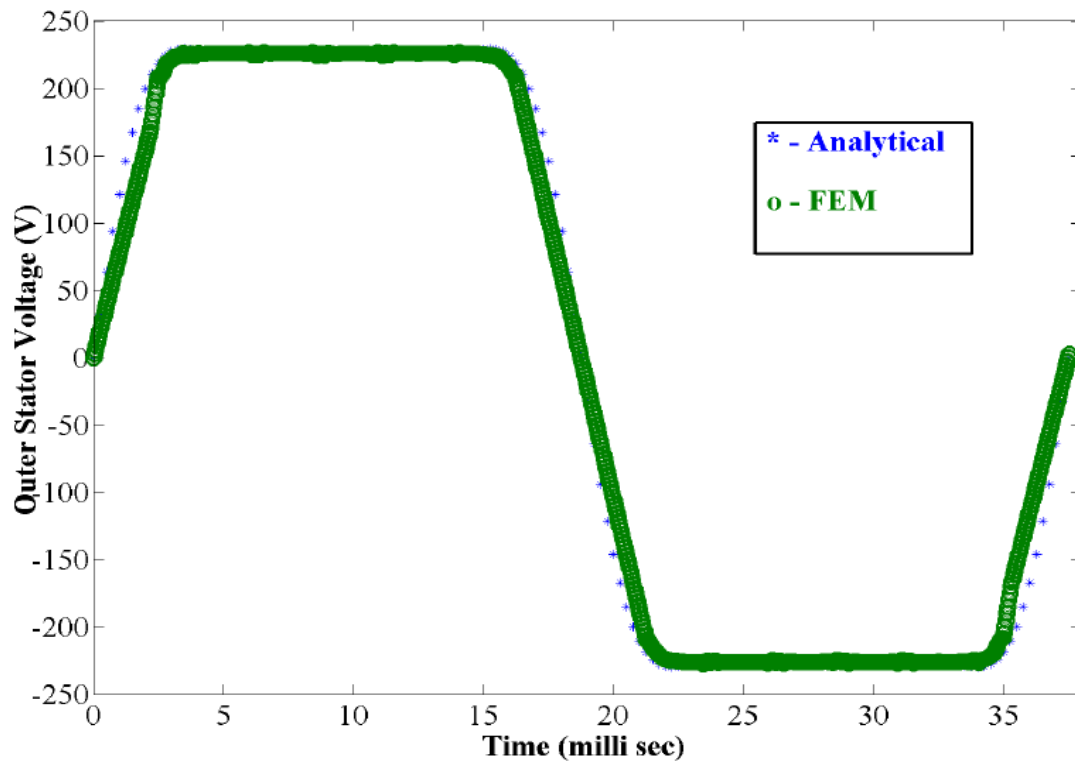Fig. 2.35 FEM and Analytical result of inner air gap flux density

Fig. 2.36 FEM and Analytical result of outer stator voltage
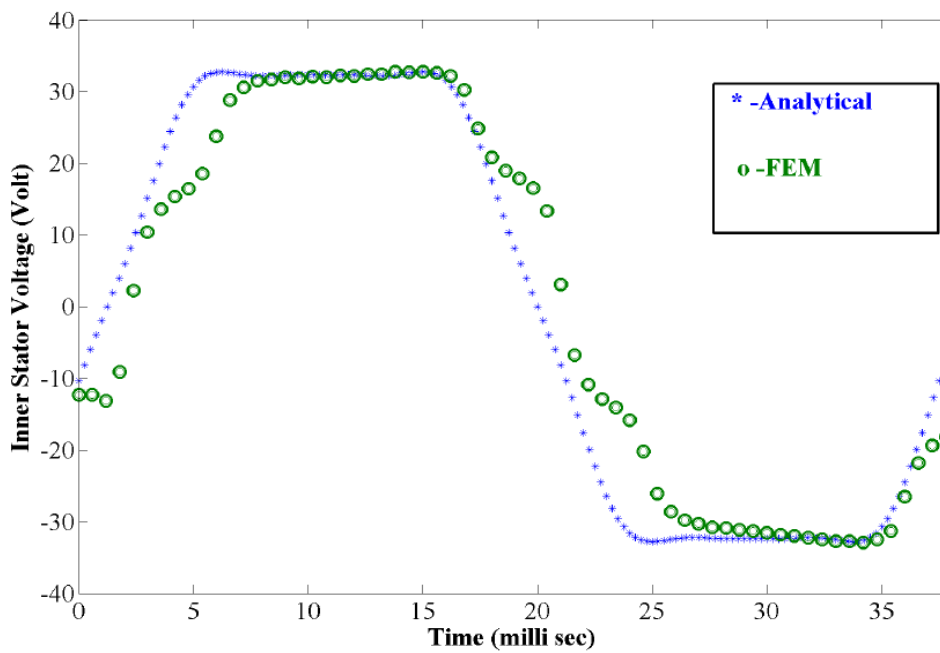

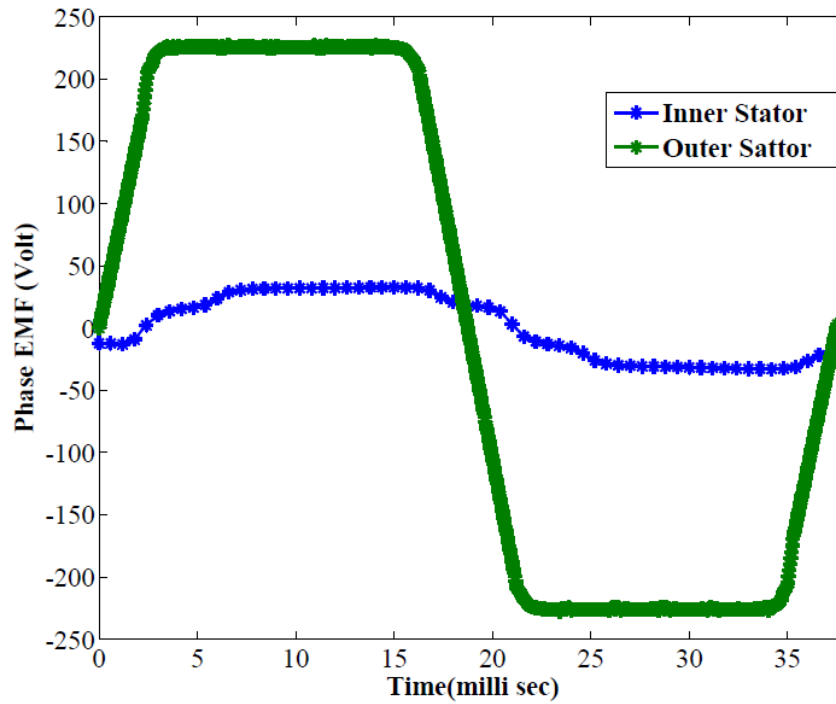Fig. 2.37 FEM and Analytical result of inner stator voltage

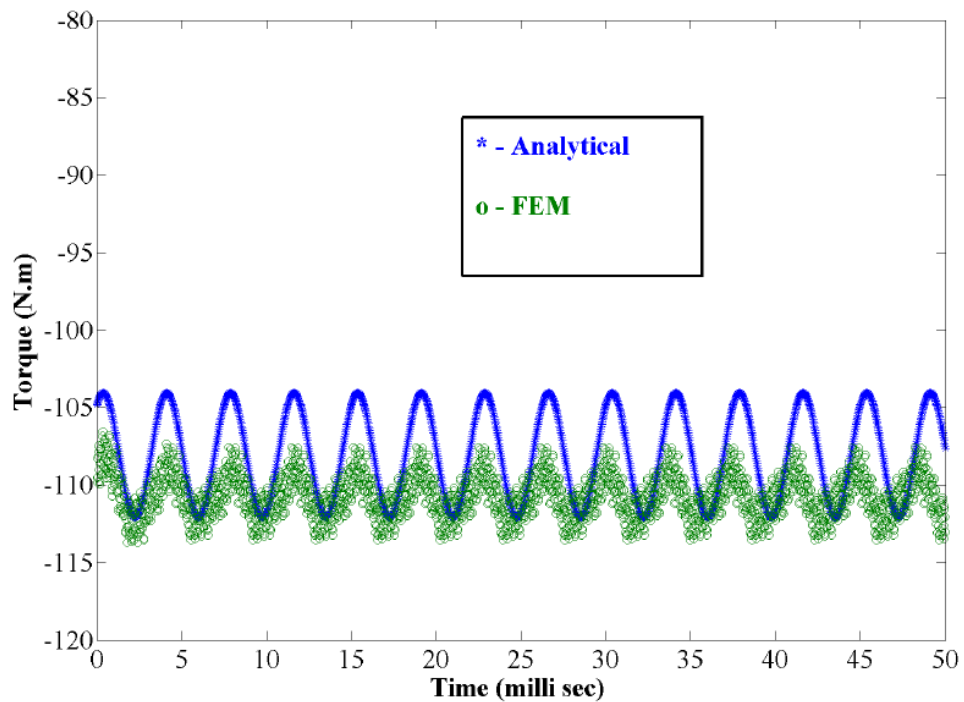Fig. 2.38 FEM inner and outer stator No-Load phase EMF

Fig. 2.39 FEM and Analytical results of electromagnetic torque

2.12. Conclusion

A comparison is made between the conventional dual stator and novel magnetically coupled dual stator PMSG and it is found that Novel magnetically coupled dual stator PMSG is better than conventional Dual stator PMSG. The magnetic circuit approach is an analytical tool for design improvement. The Improved Magnetic Circuit model (IMC) has been proposed in terms of material properties and machine dimensions for considering the design optimization of SSFP-PMSG and MCDSFP-PMSG. By the IMC it is identified that various parameters like the dimension of the permanent magnet, core material, rotor PM sleeve material directly affects the performance like generated voltage, cogging torque etc. it also suggested that the improper selection of PM dimension leads the adverse effect of saturation which de-rates the generator and increases the cost of magnets. The eddy current heat loss in the magnet is a common problem in PM machines. Magnet segmentation is required to reduce the eddy current losses. To hold the segmented magnet on the rotor surface, rotor PM sleeves are required. The rotor PM sleeves may be metallic or non-metallic. The non-metallic carbon fiber rotor PM sleeve is more suitable than metallic PM sleeve like Al, copper, magnetic-stainless steel etc; because of less electrical conductivity. This reduces the eddy current loss developed in it specifically at very high speed. However the mounting of non-metallic sleeve is very difficult. For low-speed machine, metal rotor sleeve are advantageous because of low cost, better thermal characteristic and easy installation for covering the PMs. For different applications the core material may be changed and a very low permeability material like air can also be preferred. Furthermore, it was found that every combination of slot and pole cannot give balance winding and its feasibility depends on the integral values of phase offset. The

segmented rotor limits the leakage flux and enhances the performances. The electromagnetic performance has also been carried out like generated voltage, terminal voltage, electromagnetic torque using IMC Model for MCDSFP-PMSG and all the results are verified with FEM results with errors within 5% of the predicted values. As the separation increases the local leakage flux is reduced. At the same time it starts to inject the harmonic in the generated voltage. So the design point should be carefully selected. It is also established that the interaction of the variable air-gap reluctances depends on the interaction of stator tooth and PMs. The IMC predicts the performance of the generator as a function of dimensional parameters, core and sleeve materials in less time. The Ansoft maxwell software is used for the FEM analysis. The predicted magnetic flux distribution and electromagnetic performances from an analytical method have also been validated with FEM results. In the next Chapter Fabrication has been carried out for the experimental validation of the electromagnetic performances of the proposed PMSGs.